

**ANNULAR CLEARANCE GAS SEALS IN THE 21<sup>ST</sup> CENTURY:**

**A REVIEW OF THE EXPERIMENTAL RECORD ON LEAKAGE AND DYNAMIC FORCE COEFFICIENTS, INCLUDING COMPARISONS OF MODEL PREDICTIONS TO TEST DATA**

**Luis San Andrés**

Mast-Childs Chair and Professor  
[lsanandres@tamu.edu](mailto:lsanandres@tamu.edu)

J. Mike Walker '66 Department of Mechanical Engineering  
 Turbomachinery Laboratory, Texas A&M University  
 College Station, TX 77845, USA

**Adolfo Delgado**

Associate Professor  
[adelgado@tamu.edu](mailto:adelgado@tamu.edu)



*Luis San Andrés performed research in lubrication and rotordynamics and advanced technologies for hydrostatic bearings in primary power cryogenic turbo pumps, squeeze film dampers for aircraft jet engines, and gas foil bearings for oil-free micro turbomachinery. Luis is a Fellow of ASME, STLE, GPPS, and a member of the Industrial Advisory Committees for the Texas A&M Turbomachinery & Pump Symposia. He earned a MS in ME from the University of Pittsburgh and a PhD in ME from Texas A&M University. Luis has published over 260 peer reviewed papers in various ASME journals and conference proceedings, TPS and ATPS included. Several papers are recognized as best in various international conferences. Dr. San Andrés received the ASME 2022 Aircraft Engine Technology Award for sustained personal creative contributions to aircraft engine technology.*



*Adolfo Delgado is an Associate Professor at Texas A&M University. His research focuses on rotordynamics, structural vibration, energy dissipation mechanisms, thin film lubrication and fluid structure interaction applied to the design, modeling and improvement of rotating machinery systems and components. Adolfo is a member of the Industrial Advisory Committees for the Texas A&M Turbomachinery & Pump Symposia. He has published over 40 technical papers and holds 10 patents. Adolfo received his B.S. in ME from Simón Bolívar University (Venezuela), and his M.S. and Ph.D. in ME from Texas A&M University.*

**ABSTRACT**

Turbomachinery seals are engineered to maintain efficiency and power delivery by minimizing leakage. Seals also appreciably affect the system rotordynamic behavior due to their relative position within a turbomachine. The tutorial reviews the experimental record on gas seals as published in the 21<sup>st</sup> century<sup>1</sup>, and gives insight on the physical models predicting leakage and dynamic force coefficients. Simple leakage and transport equations are the basis for bulk flow models (BFMs), whereas computational fluid dynamics (CFD) software relies on the solution of the Reynolds-Averaged Navier-Stokes equations (RANS) with an appropriate turbulence flow model in a multi-million node mesh count.

Leakage data for seals with nominal clearance ( $C_r$ ) include labyrinth and interlocking labyrinth seals, damper seals such as honeycomb (HS), pocket damper seals (PDS), conventional and hybrid brush seals, and the advanced (clearance control) HALO seal. A flow factor characterizes the seals as a single-knife (restriction) with an effective clearance ( $C_e$ ). The extensive comparisons of leakage, measured and predicted, show that engineered seals have an effective clearance  $C_e/C_r = 0.30 - 0.40$ , and which is not a function of either inlet pressure, exit pressure, rotor speed, or even actual clearance. The finding attests to the well-understood nature of the fluid flow through the seals. Both BFM and CFD models accurately predict seal leakage.

Seals produce reaction forces due to shaft lateral displacements, and with stiffness and damping coefficients characterizing a seal dynamic response. A direct stiffness ( $K$ ) produces a centering action whereas a direct damping ( $C$ ) dissipates mechanical energy. A cross-coupled stiffness ( $k$ ) arises due to shaft rotation dragging the gas around the seal circumference. In general, the force

<sup>1</sup> In 1997, Profs. John Vance and Dara Childs of the Turbomachinery Laboratory published a lecture at TPS entitled “Annular Gas Seals and Rotordynamics of Compressors and Turbines.” This tutorial emphasizes the modeling efforts and testing campaigns conducted in the 21<sup>st</sup> century.

coefficients of a gas seal are frequency ( $\omega$ ) dependent. A positive  $k$  ( $>0$ ) decreases the seal effective damping  $C_{eff} = (C-k/\omega)$ , hence degrading the stability of the mechanical element.  $k$  is proportional to the gas circumferential speed entering the seal; hence, adding either a swirl-brake or shunt-injection with (excess) gas flowing in the direction opposite to shaft rotation helps to diminish  $k$  ( $\rightarrow 0$  or negative).

The tutorial reviews multiple examples of normalized stiffness and damping coefficients for various seal types including uniform clearance seals, LS, and damper seals (HS and PDS). LS with teeth on the rotor surface are notorious for producing large  $k$ . Poorly designed LS, installed as either balance piston seals or impeller eye seals, are the cause of many rotordynamic instability fiascos. Damper seals produce direct  $K$  and  $C$  orders of magnitude larger than those from conventional LS. Damper seals in conjunction with a swirl brake also produce very small  $k$ ; hence, effectively removing a concern on rotordynamic instability. Past are the days when LS, known *bad actors*, were the only choice effectively sealing the stages in a turbomachine. Incidentally, damper seals, honeycomb and hole-pattern seals in particular, can produce a large centering stiffness ( $K \gg 0$ ) that makes a balance piston seal in a back-to-back centrifugal compressor act as a third bearing, hence rising the first natural frequency of the rotor system.

Although both the BFM and CFD models are good at predicting leakage, they fall short of replicating the experimental force coefficients of damper seals. At times,  $C$  is accurately predicted while  $K$  or  $k$  are not, or vice versa. The predictive methods still need improvement, hence the need of constant and continuous experimental verification. Differences between predictions and measured force coefficients are likely due to the lack of fidelity in reproducing complex unsteady (highly turbulent) flows whose dynamic pressure acting on the rotor produces the seal reaction force. Derived from the comprehensive experimental results, the review concludes by advancing *rules of thumb* to estimate the range of expected direct stiffness ( $K$ ) and effective damping ( $C_{eff}$ ) applicable to damper seals.

Unlike experiences in the past century, damper seals offer a remarkable opportunity to control the leakage and tailor the rotordynamic performance and stability of modern rotating machinery.

## INTRODUCTION

Turbomachinery seals are designed to maintain efficiency and power delivery by minimizing leakage. Hence, seal design is the most cost effective practice to increase performance by restricting secondary flow leakage. High performance turbomachinery operates at large rotor surface speeds (up to 400 m/s), with mechanical components withstanding high temperatures (600°C and above), and large pressure differentials to produce machines with increased power and efficiency [1]. Seals must be able to control flow while enduring severe operating conditions; hence, the need of specialized materials and configurations with demonstrated reliable performance, savings in power, and extended life.

While the primary role of annular seals is to reduce secondary or parasitic flows, they can generate large lateral forces and have a measurable impact on the rotordynamic performance of turbomachinery, particularly in centrifugal compressors and axial flow turbines. Operating characteristics unique to seals are the large axial pressure gradients and large clearance to radius ratios, while the axial development of the circumferential velocity is of importance in the generation of cross-coupled (hydrodynamic) forces [2].

Figure 1 depicts the cross-section of a compressor with shrouded impellers and the location of the seals restricting secondary leakage: impeller eye (or neck ring) and inter-stage seals on each stage, and a balance drum or piston on the right end that reacts to the thrust load produced by each stage. Figure 2 depicts a few seal types of common use in centrifugal compressor applications. In damper seals, textured stator surfaces (macro roughness) reduce the impact of undesirable cross-coupled dynamic forces and thereby improve overall rotordynamic stability.

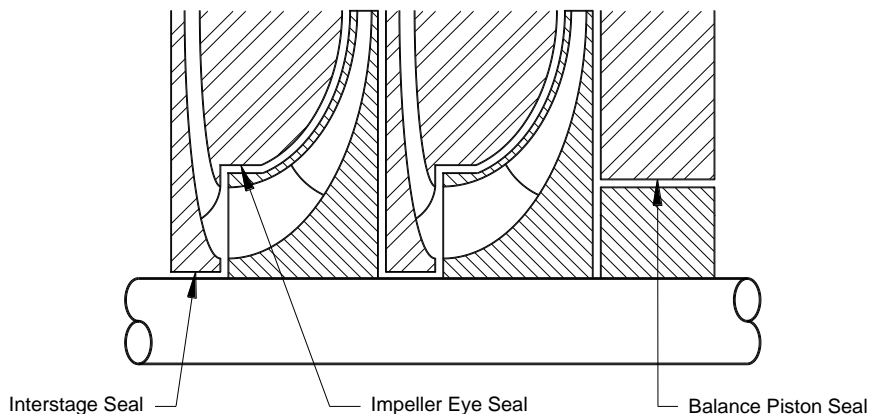


**Figure 1 Seals in a Multistage Centrifugal Pump or Compressor [2].**

Seals, due to their relative position within the rotor-bearing system, can appreciably affect the system dynamic behavior since these elements are typically located at positions which experience large amplitude rotor motions. This assertion is of particular importance in back-to-back compressor arrangements; see Figure 3 ([3]). Furthermore, the force coefficients – stiffness, damping and inertia- of annular seals in liquid pumps can be as large as those arising in the oil-lubricated bearings; thus, the seal elements effectively become load paths and modify the pump rotordynamic behavior. “Wet” and “dry” critical speeds, i.e. those accounting for seals’ forces and not, can be markedly different as noted by Black in 1969 [4].

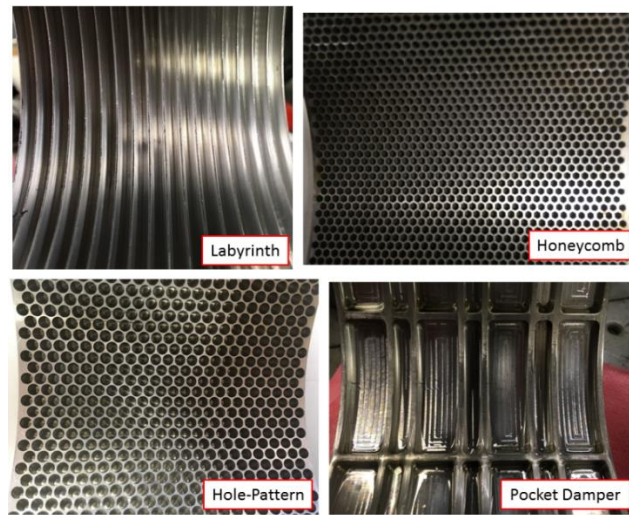


Figure 2 Photographs of a labyrinth seal (LS), a honeycomb seal (HS), a hole-pattern seal (HoS), and a fully-partitioned pocket damper seal (FPDS).

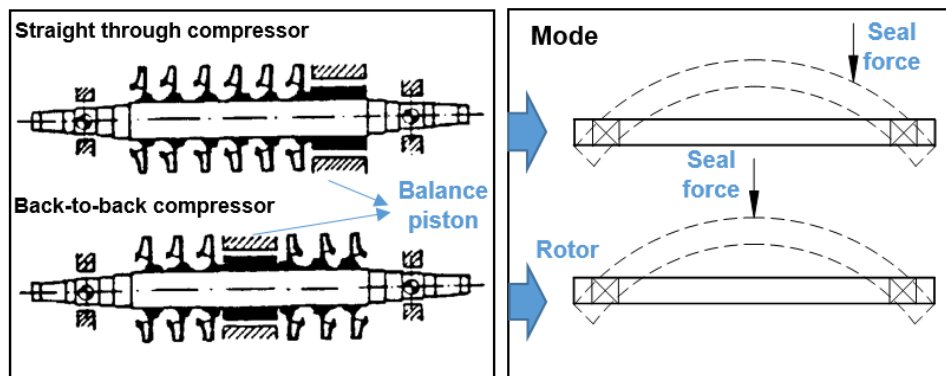


Figure 3 Straight-Through and Back-to-back Compressor Configurations and 1<sup>st</sup> Mode Shapes. Adapted from [3].

Labyrinth seals (LS) are the most common type of annular gas seal used in turbomachinery and are used as inter-stage and impeller eye seals. See Figure 4 for two depictions of LSs, one with upstream ribs for flow straightening and the other with a swirl brake, to decrease the inlet circumferential swirl of the seal. In centrifugal compressors, labyrinth seals as balance piston seals face the largest pressure differentials in the machine. Balance piston seals are located at the center of a back-to-back compressor, near the rotor mid-span, or after the last stage in a straight-through compressor; see Figure 3. Because of their location and large pressure differentials, these seals develop the largest destabilizing aerodynamic forces and directly affect the rotordynamic performance of centrifugal compressors. The magnitude of these forces is highly sensitive to the fluid density, pressure difference across the seal, and the inlet circumferential flow velocity or inlet pre-swirl ratio defined as the incoming tangential flow velocity divided by the rotor surface speed [3].

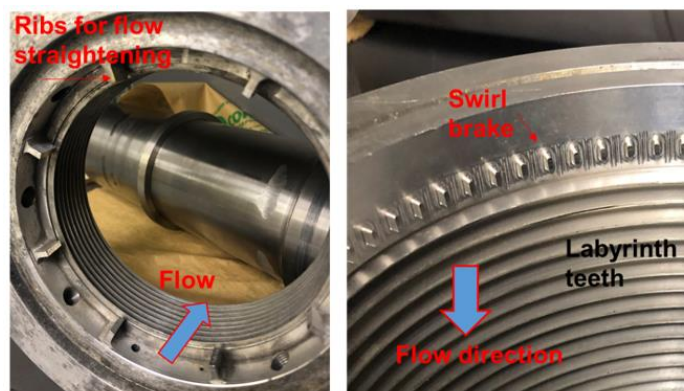


Figure 4 Photographs of two labyrinth seals, one with a swirl brake (right picture).

In 1965 Alford [5] explained two of the probable causes for self-excited rotor whirl observed in aero-engines. The first refers to a non-uniform circumferential static pressure acting on the rotor surface within seal cavities; and the second is rotor eccentricity causing an unequal circumferential tip blade clearance. The non-uniform circumferential pressure develops a tangential (destabilizing) force proportional to the radial displacement. Alford concluded that a LS having a diverging clearance (knife

clearance increases along the flow direction) is more stable than one with a converging clearance, and with rotor whirl beginning at a torque level proportional to the rotor-bearing system stiffness. Alas, Alford only accounted for axial flow in the analysis and ignored the circumferential flow. The assumption proved incorrect, as later shown by Benckert and Wachter [6], who demonstrated experimentally that circumferential flow in LSs directly affects their destabilizing forces. Experiments in [6] consisted of statically offsetting a shaft and measuring the cross-coupled stiffness coefficients for LSs (see-through and interlocking), LSs with swirl webs at the entrance plane to disrupt circumferential flow, LSs with swirl webs throughout the seal, and a honeycomb seal. Since their static load tests experimental results did not include damping coefficients, the authors recommend a LS with inlet swirl webs (i.e., a swirl brake), more so than a LS with swirl webs or a honeycomb seal, as the best option to minimize destabilizing forces.

A few years later (1982), as part of the engineering work to enable the development of turbopumps for the Space Shuttle Main Engine (SSME), Von Pragenau [7] showed that a textured (or rough) surface stator, instead of a smooth surface one, increases the drag and reduces the leakage, while also impeding the evolution of the circumferential flow and axial flow velocities. The end result is a significant improvement in rotordynamic performance. The improved rotordynamic and leakage performance also applies to compressible fluids, i.e. gases, as verified experimentally by Childs et al. [8], [9]. In addition, textured surface seals can produce large direct stiffness and damping coefficients, i.e., centering and dissipative forces that could stabilize an otherwise unstable machine.

Figure 2 also portrays other seals generally known as *damper seals* as their main function is to generate viscous damping dissipation forces besides just restricting leakage [7]. The seals depicted are a honeycomb seal (HS), a hole-pattern seal (HoS), and a fully-partitioned pocket damper seal (FPDS). As shown in Figure 5, HSs have a typical hexagon pattern with thin walls, while hole-pattern seals feature round holes with a certain depth. The area of the honeycomb cells or holes relative to the flow area and the depth of the cells (holes) relative to the clearance are of great importance (i.e., design parameters).



**Figure 5 Photographs of a honeycomb seal and a hole-pattern seal, both with swirl brakes upstream of the seal entrance.**

Similar to LSs, a pocket damper seal (PDS) includes buffer walls running axially that divide the circumferential grooves into multiple pockets. The conventional PDS dating from 1993 [10] generates damping from two distinct features. The first feature is a blades' divergent clearance along the length of the seal. The second feature is the buffer walls that isolate the pockets and reduce the swirl of the circumferential flow. The PDS proved to have significantly more (viscous) damping than does a traditional LS.

In 1997, Childs and Vance [11] reviewed annular gas seals for compressors and turbines and provided details of their effect on the rotordynamics of turbomachinery. At the time, damper seals including HSs, PDSs, brush seals (BS), and LSs with swirl brakes and shunt injection were already being used to improve the stability of rotating machinery equipment with demonstrated savings in leakage performance. The earlier view that labyrinth seals were *bad actors* that caused rotordynamic instability problems had changed to make damper seals engineered mechanical elements with the ability to improve the rotordynamic response and stability of turbomachinery.

## PREDICTION OF LEAKAGE IN ANNULAR CLEARANCE SEALS

The most important function of a seal is to restrict, even eliminate, the secondary flow from a high pressure zone into a low pressure zone. Hence, accurate prediction of the seal leakage is an important engineering design practice. As shown in Figure 6 depicting various types of labyrinth seals, the flow moves through a tortuous path and displays two regimes; namely a core flow and recirculation zones in the deep cavities. The core flow is a jet through flow along the leakage path. The recirculation zones in a cavity contribute to mechanical energy dissipation, and hence leakage reduction.

Clearly, the annular gap or clearance ( $C_r$ ) between the seal stator and the spinning rotor is the most important physical parameter. That is, tight clearances are preferred since the leakage is low. Inevitably due to wear during low speed (slow roll during start up) operation, the clearance will grow and the leakage will rise. Hence, seals are designed to still restrict leakage when their clearances double ( $2 C_r$ ).

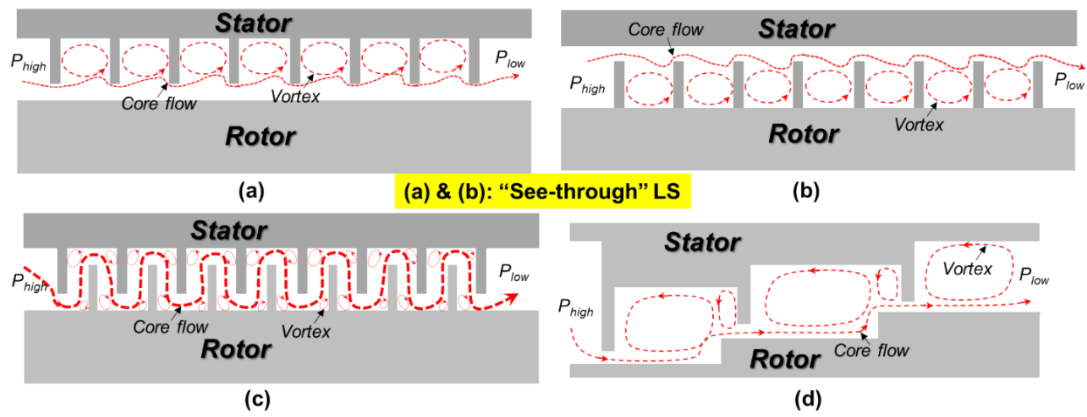


Figure 6 Schematic views of flow passing through the clearance channel in a seal: (a) teeth on stator (TOS), (b) teeth on rotor (TOR), (c) interlocking labyrinth seal (ILS), and (d) stepped LS.

Methods to calculate (predict) leakage range from simple algebraic equations relating the flow rate to a pressure drop, to bulk-flow models (BFM) with two-dimensional transport equations governing the fluid motion along the axial and circumferential directions; and more recently, to computational fluid dynamics (CFD) three dimensional (3D) models that include advanced turbulent flow models. CFD models demand fine meshes with millions of nodes and are computationally intensive. Nonetheless, commercial CFD software are readily available and have become ubiquitous in the routine engineering practice. Figure 7 summarizes the major advantages and disadvantages of CFD methods vs. BFM. One must expect the speed of computer processors to keep increasing; hence in the near future, fluid flow-deformable solid interaction models will be conducted routinely and in real time.

|                       | Pros 👍  | Cons 🗨️   |
|-----------------------|---|---|
| Bulk-Flow Model (BFM) | <ul style="list-style-type: none"> <li>✓ Quick</li> <li>✓ Easy set up</li> </ul>                                | <ul style="list-style-type: none"> <li>❑ Lacks enough accuracy</li> <li>❑ Needs empirical coefficients</li> </ul>     |
| CFD                   | <ul style="list-style-type: none"> <li>✓ High fidelity</li> <li>✓ No empirical coefficients required</li> </ul> | <ul style="list-style-type: none"> <li>❑ Computationally expensive</li> <li>❑ Requires knowledge about CFD</li> </ul> |

Figure 7 CFD methods vs. bulk flow models: a brief take on their pros' and cons'.

As an example, Figure 8 shows schematic views of an interlocking labyrinth seal (ILS) with clearance  $C_r$  and rotor radius  $R_s$ . Knives on both the rotor and the stator have the same geometry. The flow domain consists of  $n$  cavities separated by blades, a total of  $N_T = n+1$ , and where  $B$  and  $L_i$  denote the knife height and pitch or cavity width. Within the  $i^{\text{th}}$  cavity, the pressure is  $P_i$  and the mean circumferential velocity is  $U_i$ . Assuming an ideal gas, its density  $\rho_i = P_i / (Z_g R_g T)$ , where  $R_g$  and  $Z_g$  are the gas constant and the compressibility factor, and  $T$  is the gas temperature.

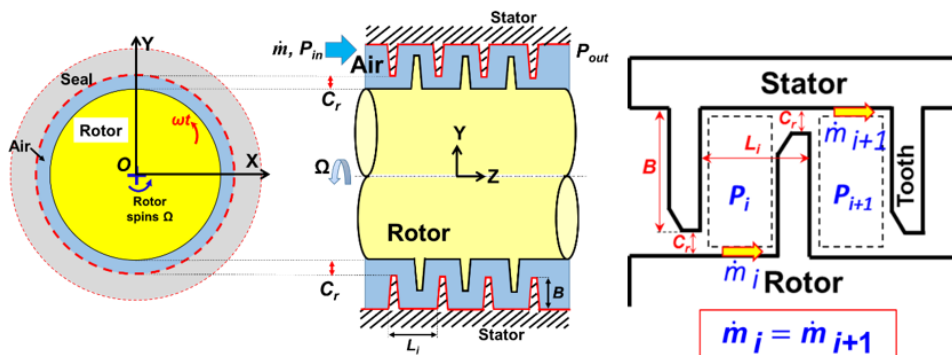


Figure 8 Schematic views (not to scale) of an interlocking labyrinth seal (ILS) and an one-control-volume model.

The BFM analysis of leakage in LSs incorporates the well-known Neumann's equation [3] that relates the mass flow rate  $\dot{m}$  through a single knife as a function of the difference in upstream and downstream cavity pressures,  $P_{i-1}$  and  $P_i$ , i.e.<sup>2</sup>

$$\dot{m}_i = \pi D \bar{m}_i = \mu_{i1} \mu_{i2} (\pi D C_r) \sqrt{\frac{P_{i-1}^2 - P_i^2}{R_s T}} \quad (1)$$

$\bar{m}$  is the mass flow rate per circumference length. Above  $\mu_{i2}$  is a flow discharge coefficient and  $\mu_{i1}$  is the kinetic energy carry-over coefficient. Note that  $\dot{m} = \dot{m}_1 = \dot{m}_2 = \dots = \dot{m}_{NT}$ , i.e., the flow under every knife is the same. Formulas for the  $\mu$  coefficients are [12]:

$$\mu_{i2} = \frac{\pi}{\pi + 2 - 5\beta_i + 2\beta_i^2} \leftarrow \beta_i = \left(\frac{P_{i-1}}{P_i}\right)^{\frac{\gamma-1}{\gamma}} - 1 \quad (2)$$

where  $\gamma$  is the ratio of specific heats. For air,  $\gamma=1.4$ . For a *see-through* LS, TOR or TOS, the kinetic energy carry-over coefficient ( $\mu_{i1}$ ) is a function of the seal geometry

$$\mu_{i1} = \left(\frac{NT}{(1-\lambda)NT + \lambda}\right)^{\frac{1}{2}} \leftarrow \lambda = 1 - (1 + 16.6 C_r / L_i)^{-2} \quad (3)$$

For the first knife in a *see-through* LS and all the teeth in an ILS,  $\mu_{i1} = 1$  [3]. Note  $\lambda$  is constant in a seal with uniform spacing of the knives (cavity widths and depth).

In a single control-volume BFM, the conservation of mass and circumferential momentum transport equations are [3]

$$\frac{\partial(\rho_i A_i)}{\partial t} + \frac{\partial(\rho_i U_i A_i)}{R_s \partial \theta} + \bar{m}_{i+1} - \bar{m}_i = 0 \quad (4)$$

$$\frac{\partial(\rho_i U_i A_i)}{\partial t} + \frac{\partial(\rho_i A_i U_i^2)}{R_s \partial \theta} = -\frac{A_i}{R_s} \frac{\partial P_i}{\partial \theta} + (\tau_r a_r - \tau_s a_s) L_i \quad (5)$$

Above,  $U_i$  and  $P_i$  are the circumferential velocity and pressure in a cavity,  $A_i = (B + C_r) L_i$  is the area of a cavity cross-section, and  $(\tau_r, \tau_s)$  are the wall shear stresses acting on the rotor and stator. For a TOR LS,  $a_r = (2B + L_i) / L_i$ ,  $a_s = 1$ ; whereas for a TOS LS:  $a_r = 1$ ,  $a_s = (2B + L_i) / L_i$ . Since an ILS has knives both on the stator and rotor,  $a_r = a_s = (B + L_i) / L_i$ . The shear ( $\tau$ ) stresses are a function of friction factors whose magnitude depends on the flow conditions, i.e., the Reynolds numbers. See [3] for more details.

The literature also presents more complex BFMs that account for two control volumes, one in the circulation zone within a cavity, and the other in the jet flow region extending from a knife-edge [13]. A three control volume model includes the flow area under a knife. Figure 9 depicts schematic view of the various control volumes. These models are not described here due to brevity.

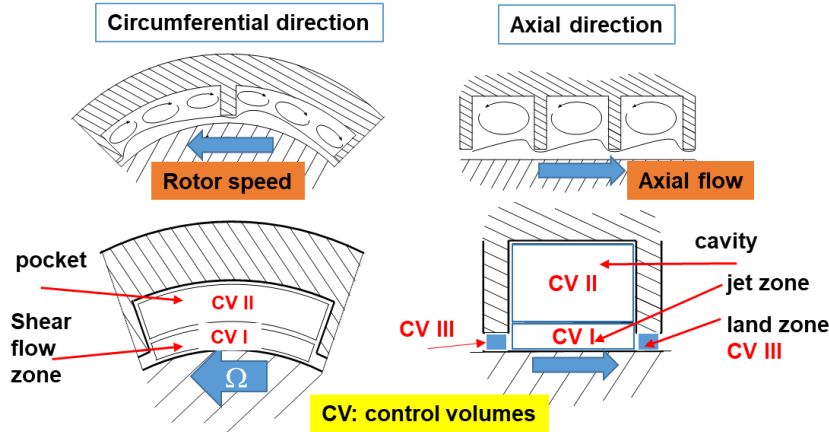


**Figure 9** Schematic views of the flow patterns and control volumes for the BFM in labyrinth seals (LS) and pocket damper seals (PDS). Taken from [13].

The BFM equations are solved numerically with appropriate boundary conditions, namely the inlet pressure ( $P_{in}$ ) and the circumferential swirl velocity ( $\alpha \Omega R_s$ ) at the seal inlet plane, and the exit pressure ( $P_{out}$ ) at the exit of the seal. It is highly desirable a LS operates unchoked, i.e. with flow conditions well below a Mach number =1. For a uniform clearance LS, this condition is easily satisfied when

$$\frac{P_{in}}{P_{out}} < r_c = \left(\frac{\gamma+1}{2}\right)^{\frac{\gamma}{\gamma-1}} \sqrt{b_1 \mu_i^2 + b_1 (NT - 2) + 1} \leftarrow b_1 = 1 - \left(\frac{\gamma+1}{2}\right)^{\frac{2\gamma}{\gamma-1}} (=0.721, \text{ for air}) \quad (6)$$

<sup>2</sup> The published literature offers other distinct equations for the flow of a gas through a restriction; in particular, formulas derived from gas dynamics (isentropic flow). The concept of an effective clearance is most useful to characterize the effectiveness of brush seals, see [1], [32].

Note the critical pressure ratio ( $r_c$ ) is a function of the number of knives ( $NT$ ). Increasing the number of knives raises  $r_c$ .

In a CFD model, the first step is to create a mesh that accommodates the geometric features of the seal studied. Figure 10 depicts the computational domain and corresponding mesh for a TOS labyrinth seal with uniform radial clearance. The total number of nodes equals 8.7 million. Note the physical scales of the knives, length and pitch, are much larger than the clearance; hence the need to produce dense meshes in the flow region spanning the seal clearance. Since knowledge of the flow conditions entering the seal is rather incomplete, there is the need to model an upstream section whose length will determine the smooth evolution of a specified stagnant flow field at the inlet of the flow region. Similarly, a flow extension at the exit is often required to specify a constant (exit) pressure well after the physical length of the seal ends.

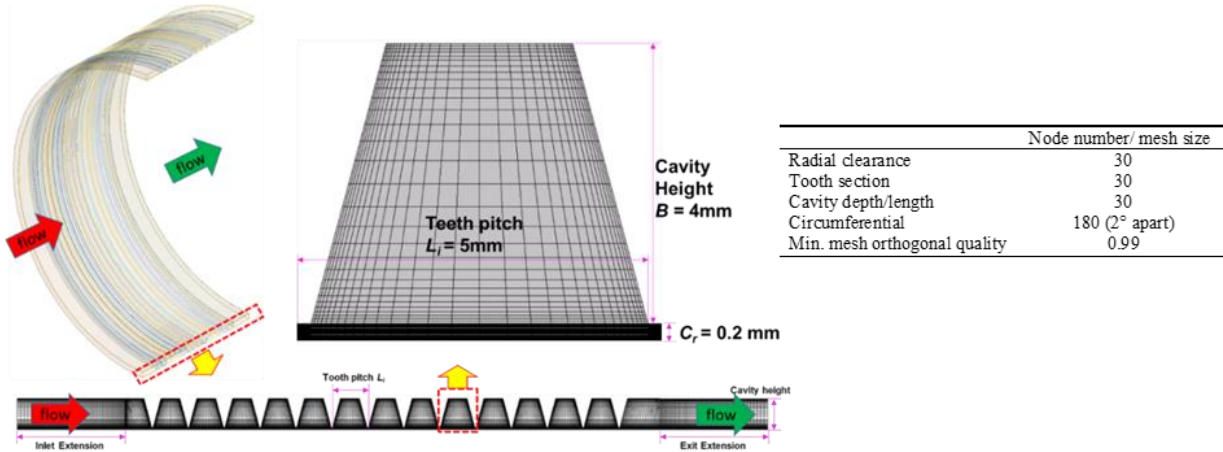


Figure 10 CFD mesh for a knives on stator (TOS) labyrinth gas seal.

To date, both the generation of a fine enough mesh and the selection of the appropriate flow model, laminar or turbulent, remain critical for the CFD software to produce accurate results, insensitive to a further refinement of the mesh, and evidencing significant flow characteristics such as regions with intense energy dissipation. The flow across an annular clearance seal is highly turbulent due to the low viscosity ( $\nu = \mu/\rho$ ) of the gas, the seal's large radial clearance<sup>3</sup>, the high speed of the rotor surface ( $U_s = \frac{1}{2} D\Omega$ ), and the significant pressure differential  $\Delta P = (P_{in} - P_{out})$  that produces a large axial speed ( $W$ ). Both the circumferential flow Reynolds number ( $Re_\theta = U_s C_r/\nu$ ) and the axial flow Reynolds number ( $Re_z = W C_r/\nu$ ) are greater than 2,000; hence the fluid flow is fully turbulent [14], [15].

A turbulent flow condition is one where the flow properties, velocity and pressure fields, comprised of mean values ( $u$ ) and fast unsteady fluctuations ( $u'$ ) that are too small in the physical scale for accurate solution with the finest mesh. Commercial CFD software offers a choice of turbulent flow solvers for the Reynolds-Averaged Navier-Stokes (RANS) Equations. These are momentum transport and flow continuity equations for the mean or average fluid velocity components ( $u_{x,y,z}$ ) and pressure field, and particular transport equations modeling specific features of the turbulent flow. These features include the kinetic energy ( $\kappa$ ) of the fluctuations, their energy dissipation ( $\epsilon$ ), the specific dissipation rate ( $\omega = \epsilon/\kappa$ ); and in more advanced cases the six components of the Reynolds stress tensor  $\left( -\rho \overline{u'_i u'_j} \right)_{i,j=x,y,z}$  [15].

Figure 11 depicts a selection of flow models typically offered by a commercial software [16] [17]. The choice models given are poorly described and the end user must judiciously select options and constants associated to the model. More often than not, the selection determines the ultimate outcome; either physically correct or not. Since 1980, chosen for expedience in calculations, commonly used models include a one-equation model (Spalart-Allmaras) and the two-equation models,  $\kappa-\epsilon$  or  $\kappa-\omega$ . There is no straight (direct) answer on which turbulence flow model is the best option in analyzing the flow in annular (gas) seals. Experimental validation of turbulent flow models is still an on-going research [18] [19] [20].

At this time, practitioners of the art of CFD modeling of gas and liquid seals recommend using either the  $\kappa-\omega$  SST (shear stress transport) model or the realizable  $\kappa-\epsilon$  model, both with the curvature correction function that makes the model predictions less sensitive to the streamline curvature and the (shaft) rotation [21]. When confronted with difficulties in convergence, the standard  $\kappa-\epsilon$  model appears to be a good option [22].

<sup>3</sup> Annular seals have typically clearances larger than those in a journal bearing; ratios  $\frac{1}{2}D/C_r = 200-500$  are common.

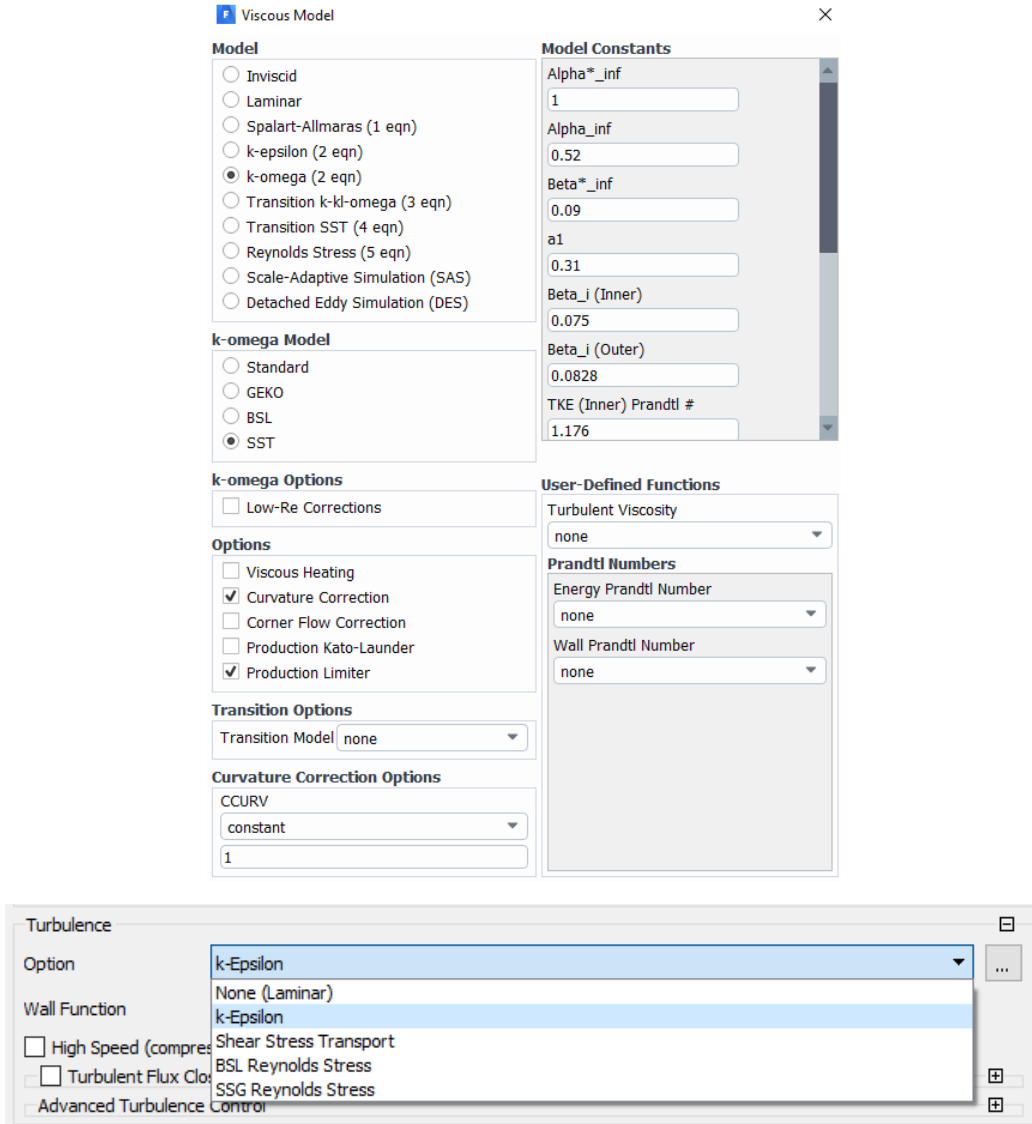


Figure 11 Screenshots of turbulence flow models offered by commercial CFD software [16], [17].

From the theory of turbulent flow [14], the flow near a wall comprises a viscous sublayer extending to  $y^+ < 5$ , then a buffer layer ( $5 < y^+ < 30$ ), and an inertia sublayer ( $y^+ > 30$ ). Here,  $y^+ = (u_\tau y/\nu)$  is a dimensionless distance from the wall where  $u_\tau = \sqrt{\tau_w/\rho}$  is a friction velocity derived from the wall shear stress ( $\tau_w$ ). Resolving the flow within the scale of the viscous sublayer demands a refinement of the mesh near a wall, and which can significantly increase the computational cost. Another option is to adopt a wall function, which models the flow near a wall, both the viscous sublayer and the buffer layer, through a semi-empirical equation. Distinct wall functions have various requirement for  $y^+$ . For example, the standard wall function requires  $30 < y^+ < 300$ , while the scalable wall is more flexible, good for a wide range of  $y^+ < 300$ . A recommendation for generating the mesh near a wall is to start with the first layer of the mesh at  $y \sim 10 \mu\text{m}$ . For instance, a proper start could be to distribute 21 mesh nodes uniformly for an annular seal with clearance  $C_r = 200 \mu\text{m}$ . Upon completion of a first numerical solution, the CFD predicts  $y^+$  on the wall; and the user can adjust the mesh nodes distribution accordingly. However, note that because a seal clearance  $C_r \ll L, D$ , the mesh refinement across the seal gap produces a highly distorted mesh; the size of the cells is (by necessity) much larger along the seal axial and circumferential directions. In the end, the node count for the mesh modeling a seal structure can be several million large; see Figure 10.

The execution of a CFD program for analysis of flow in a seal often takes many CPU hours of execution; and more often than not, produces end results (leakage for example) with little to no difference relative to the result of a simple engineering calculation.

**CHARACTERIZATION OF SEAL LEAKAGE WITH A FLOW FACTOR AND AN EFFECTIVE CLEARANCE: MEASUREMENTS VS. PREDICTIONS**

Made popular by Proctor and Delgado [23], the flow factor  $\phi = \frac{\dot{m}\sqrt{T}}{D P_{in}}$  quantifies the leakage ( $\dot{m}$ ) in a manner that shows independence of the seal size (diameter  $D$ ) and inlet flow conditions, namely pressure ( $P_{in}$ ) and temperature ( $T$ ).  $\phi$  also serves to

compare the effectiveness of various seal types. Note  $\phi$  has physical units  $\left[ \frac{\text{kg} \sqrt{\text{K}}}{\text{MPa} \cdot \text{m} \cdot \text{s}} \right]$ , i.e., strictly it is not a dimensionless parameter. Note that a modified flow factor  $\bar{\Phi} = \frac{\phi}{\sqrt{1-PR^2}}$ , with  $PR = (P_{out}/P_{in})$ , is more relevant as it accounts for the actual pressure difference across the seal.

The concept of the flow factor ( $\phi$ ) can be extended to deliver an actual dimensionless orifice-like loss coefficient for the seal. To this end, consider the flow of an ideal gas across a single restriction (knife edge) with area  $A = (\pi D C_e)$ , where  $C_e$  is an effective (radial) clearance, as shown in Figure 12. In the figure, the seal on the left is an interlocking labyrinth seal (ILS), whereas the one on the right is its equivalent representation as a single restriction seal with an effective clearance.

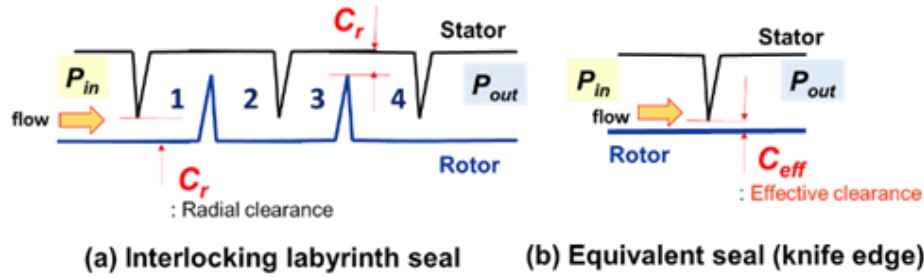


Figure 12 Schematic view of (a) ILS and (b) an equivalent seal (single knife) with an effective clearance.

Using Bernoulli's formula for the flow of an inviscid fluid, the pressure drop ( $P_{in} - P_{out}$ ) along a streamline produces a change in flow speed ( $v$ ); hence,  $\frac{1}{2} \rho v^2 \sim (P_{in} - P_{out})$ . Manipulation of this equation produces

$$\dot{m} = \rho A v = (\pi D C_e) \sqrt{2 \rho (P_{in} - P_{out})} = (\pi D C_e) \frac{P_{in}}{\sqrt{R_g T}} \sqrt{1 - PR^2} \quad (7)$$

From which the seal effective clearance ( $C_e$ ) follows as

$$C_e = c_d C_r = \frac{\dot{m} \sqrt{R_g T}}{\pi D P_{in} \sqrt{1 - PR^2}} = \frac{\sqrt{R_g T} \bar{\Phi}}{\pi} \quad (8)$$

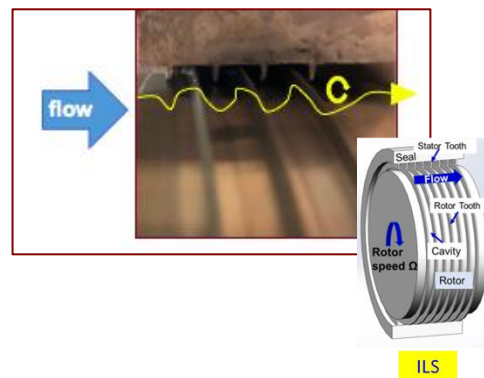
with  $c_d$  as an orifice-like (non-isentropic) loss coefficient. That is, since  $c_d < 1$ ,  $C_e$  is a fraction of the seal nominal clearance  $C_r$ .

### Leakage of Interlocking Labyrinth Seals

Consider the seal in Table 1 that shows a five-knived, ILS and operating conditions that include large variations in pressure and rotor speed. The seal has three knife-edges on the stator and two similar knives on the rotor, thus creating four cavities of 8.3 mm width and 5.8 mm in depth. In the experiments, three rotors were used that produced radial clearances ( $C_r$ ) = 0.3, 0.2 and 0.13 mm. Ref. [24] describes the test rig, test seals, and swirl brakes installed upstream of the seals. The measurements included leakage, inlet and exit pressures and temperatures, inlet swirl velocity, and static pressures in the seal cavities.

Table 1 Interlocking labyrinth seal geometry and operating conditions [24].

|                |                                       |   |
|----------------|---------------------------------------|---|
|                | Rotor Diameter, $D$                   | 150 mm                                  |
| Seal           | Overall length, $L$                   | 45 mm                                   |
| Geometry       | Radial clearance, $C_r$               | 0.13, 0.2, 0.3 mm                       |
|                | Width at tip, $B_t$                   | 0.25 mm                                 |
| Air Properties | Density, $\rho$ @25 °C                | 1.2 kg/m <sup>3</sup>                   |
|                | Temperature, $T$                      | 297 K                                   |
|                | Sound speed, $a_s$                    | 314 m/s                                 |
|                | Kinematic viscosity, $\nu$            | 1.86×10 <sup>-5</sup> m <sup>2</sup> /s |
|                | Inlet pressure, $P_{in}$              | 292 ~ 1,150 kPa                         |
|                | Pressure ratio, $PR = P_{out}/P_{in}$ | 0.3, 0.5, 0.8                           |
|                | Rotor speed, $\Omega$                 | 0, 3, 5, 7.5, 10 krpm                   |
|                | $\frac{1}{2} D \Omega_{max}$          | 0 ~ 79 m/s                              |



For the 0.2 mm clearance seal, Figure 13(a) depicts the measured flow rate vs. the pressure difference ( $\Delta P = P_{in} - P_{out}$ ) for operation at three shaft speeds and three pressure ratios. The flow rate is low for the condition of a high pressure ratio ( $PR = P_{out}$

$/P_{in} \rightarrow 1$ ) and increases as  $PR$  decreases. For a fixed  $PR$ , the flow rate increases linearly with  $\Delta P$ , regardless of the rotor speed or the inlet pressure magnitude ( $P_{in} = 292 \sim 1,150$  kPa); even for  $PR = 0.3$  when the seal flow chokes at the last cavity. The measurements show that an increase in rotor speed, from 0 krpm  $\rightarrow$  10 krpm (79 m/s surface speed), decreases the flow rate by just  $\sim 3\%$ .

For operation at a constant shaft speed of 7.5 krpm (59 m/s rotor surface speed), Figure 13(b) depicts a comparison of the measured flow rate against predictions from a CFD analysis and a bulk-flow model (BFM). The modeling tools use as an input the measured inlet circumferential swirl speed  $U_{swirl}$ . Note the largest  $U_{swirl} \sim 70$  m/s. In the analysis, either a null or an imposed large swirl speed make little difference on the predictive seal leakage. Thus, the measurements attest to the validity of Neumann's equation.

Note the BFM and CFD models are both accurate; however, CFD allows scrutiny of the whole flow field, as shown in Figure 14, for the low  $PR=0.30$ , that evidences choking of the gas flow just downstream of the inlet to the last knife.

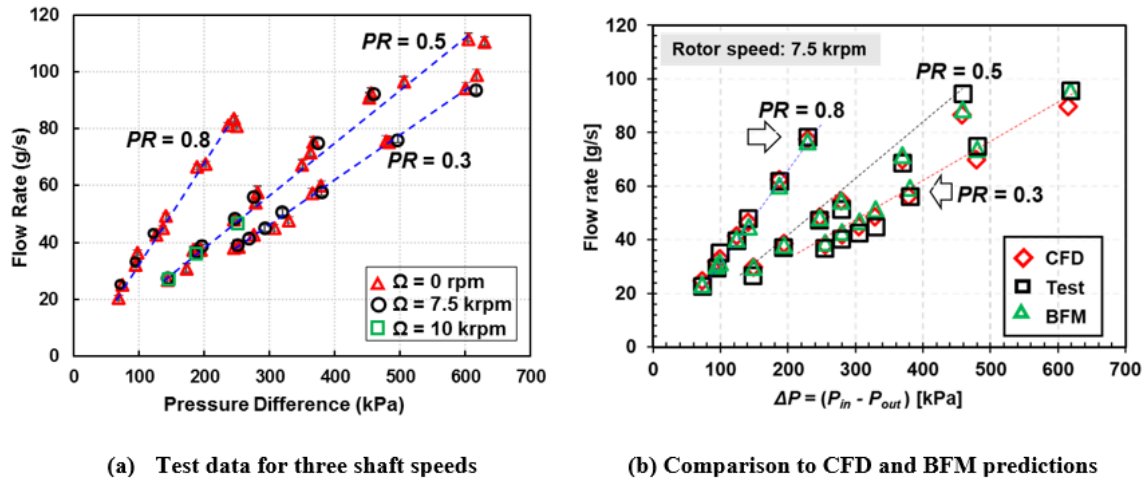


**Figure 13 Interlocking LS: measured mass flow vs. pressure difference ( $P_{in}-P_{out}$ ) for operation at pressure ratio  $PR = P_{out}/P_{in} = 0.3, 0.5, 0.8$ . Clearance  $C_r = 0.2$  mm. (a) Rotor speed  $\Omega = 0, 7.5, 10$  krpm, (b) CFD and BFM predictions vs. test data obtained at rotor speed  $\Omega = 7.5$  krpm ( $\frac{1}{2}D\Omega = 59$  m/s) [24].**

Lastly, Figure 15 portrays the modified flow factor ( $\bar{\Phi}$ ) vs.  $P_{in}$  for the three test seals. The data includes rotor speeds (to 10 krpm) and three  $PR=0.3, 0.5$  and  $0.80$ . The test results for each seal collapse into distinctive magnitudes and equal to (on average)  $\bar{\Phi} \sim 19.6, 12.8$  and  $7.8$  [ $kg \sqrt{K} / (MPa \cdot m \cdot s)$ ] for seals with  $C_r = 0.3$  mm,  $0.2$  mm, and  $0.13$  mm, respectively<sup>4</sup>. The results lie within narrow bands in spite of the swirl brake configuration, rotor speed, and inlet and exit pressures. Hence, regardless of the operating conditions, the whole set of measurements delivers a nearly unique loss coefficient ( $c_d$ ). For the ILS with  $C_r = 0.3$  mm, the test  $c_d = 0.36 \pm 0.01$ , whereas  $c_d = 0.37$  from the predictions; for  $C_r = 0.2$  mm, the experimental  $c_d = 0.36$ , whereas the predicted  $c_d = 0.35$ ; and for  $C_r = 0.13$  mm, the test  $c_d = 0.33$  while the predicted  $c_d = 0.34$ .

The measurements and predictions thus show the seal effective clearance ( $C_e$ ) is  $\sim 34\%$  of the actual operating clearance ( $C_r$ ). More importantly, the loss-coefficient  $c_d$  is not a function of the operating conditions. This is particularly important as an empirical evaluation campaign for a LS would require of a few leakage measurements, most without shaft rotation and under a moderate pressure ratio,  $PR \sim 0.6$  or so.

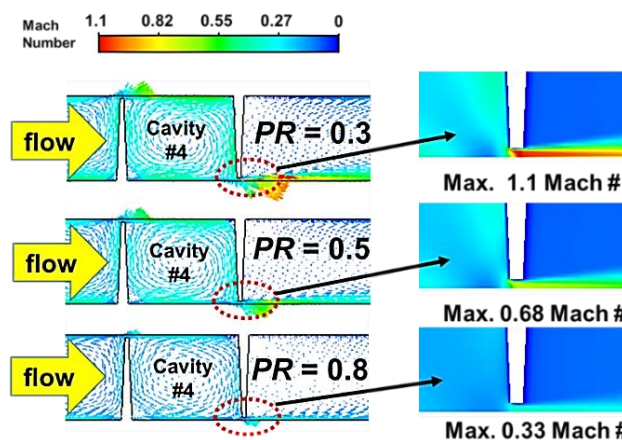


**Figure 14 CFD flow field in last cavity of ILS and Mach number. Seal operates at  $P_{in} = 363$  kPa,  $PR = 0.3, 0.5, 0.8$ , and rotor speed  $\Omega = 7.5$  krpm ( $\frac{1}{2}D\Omega = 59$  m/s). Clearance =  $0.2$  mm [24].**

<sup>4</sup> Note that portraying the flow factor ( $\phi$ ) alone shows the data has a strong variation with the pressure ratio ( $PR$ ).

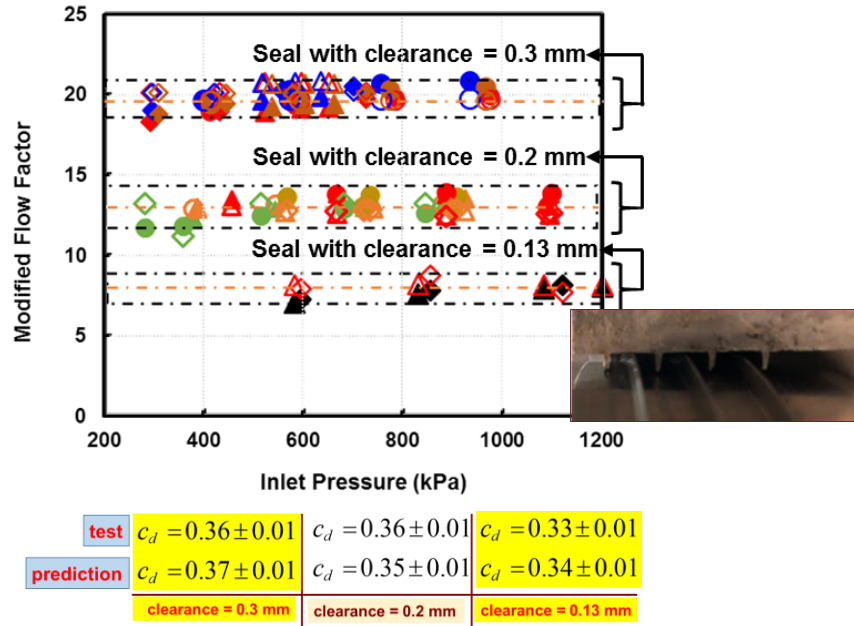


Figure 15 Modified flow factor ( $\bar{\Phi}$ ) versus inlet pressure  $P_{in}$  for three test ILs with distinct clearances [24].

### Leakage for various Short Length Seals at High Temperature

Brush seals (BS) replace LSs in aero-derivative gas (and steam) turbines demanding savings in space and efficiency. A well designed BS leaks  $\sim 1/4$  to  $1/10$  of the through flow in comparably sized LS, and will not induce rotordynamic instability. Hence, brush seals can increase plant efficiency by up to one-sixth of a point [1].

A hybrid brush seal (HBS) reduces leakage by 36% when compared to a 1<sup>st</sup> generation BS of the same size. The HBS design having a larger axial stiffness allows withstanding higher pressure differentials; however, the seal produces a larger drag torque under unpressurized conditions such as those during machine start-up and shut-down as the gas film is lost and contact ensues with the rotor. The hydrostatic advanced low leakage (HALO®) seal further evolves from the HBS with a self-controlling clearance feature as the pressure differential increases. In laboratory measurements [25], this advanced pressure seal produces  $\sim 13\%$  of the leakage in a LS at 30 °C and  $\sim 17\%$  at 300 °C. The HALO® seal works best under a choked flow condition, hence its applicability under pressure differentials a LS cannot hold and where its leakage would be excessive.

Short length labyrinth type seals are preferred on the rim side of axial flow turbines. Metal brush seals are also a known choice, while clearance control seals are more recent alternative. Figure 16 portrays four seals whose leakage was measured at a high temperature (300 °C). In the experiments reported in Refs. [25] and [26], the rotor diameter is  $D = 167$  mm and the rotor speed reached 2,700 rpm (disk surface speed = 23.6 m/s). The LS has three sharp knives, a total length of 8.4 mm and a *cold* radial clearance = 0.260 mm (0.475 mm at 300 °C). The Haynes-25 brush seal and the hybrid brush seal, with 45° bristles lay angle and a density of 850 bristles/cm, were designed to have a 0.26 mm clearance. Evolving from a hybrid brush seal, the hydrostatic advanced low leakage or HALO® seal<sup>5</sup> offers a self-controlling clearance that closes as the pressure differential increases. The HALO® seal [27] [28] has 9 arcuate pads, 40° in arc extent and 8.05 mm in axial length. Its clearance = 0.215 mm at 300 °C.

Figure 17 depicts the measured mass flow and  $\bar{\Phi}$  vs.  $P_{in}$  for the four test seals. Note  $P_{out} = 1$  bar. The LS shows the largest leakage and the smallest range of sealing pressures. Not surprisingly, the HALO® seal does the best, i.e. it restricts leakage the most. From  $\bar{\Phi}$ , the effective clearance and the seal orifice-like loss coefficient ( $c_d$ ) follow. In average,  $c_d=0.78$  for the LS,  $c_d=0.49$  for the brush seal,  $c_d=0.34$  for the hybrid brush seal, and  $c_d=0.16$  for the HALO® seal. The experimental results make evident the choice of an advanced seal configuration to restrict leakage and improve the efficiency of the rotating system.

<sup>5</sup> Other advanced concept seals include the Pressure Actuated Leaf Seal (PALS) and finger seals. See [1] for example.

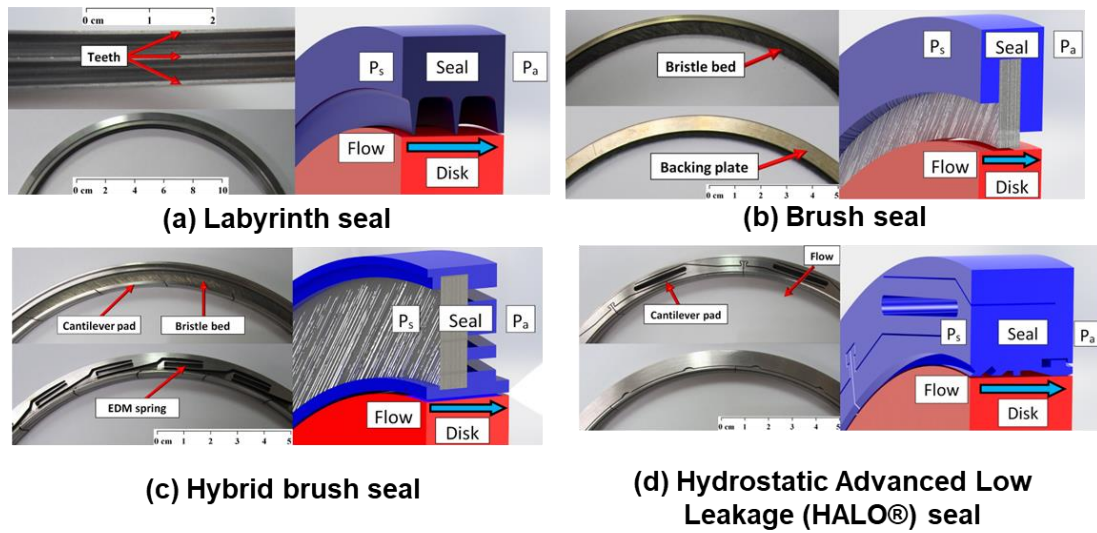
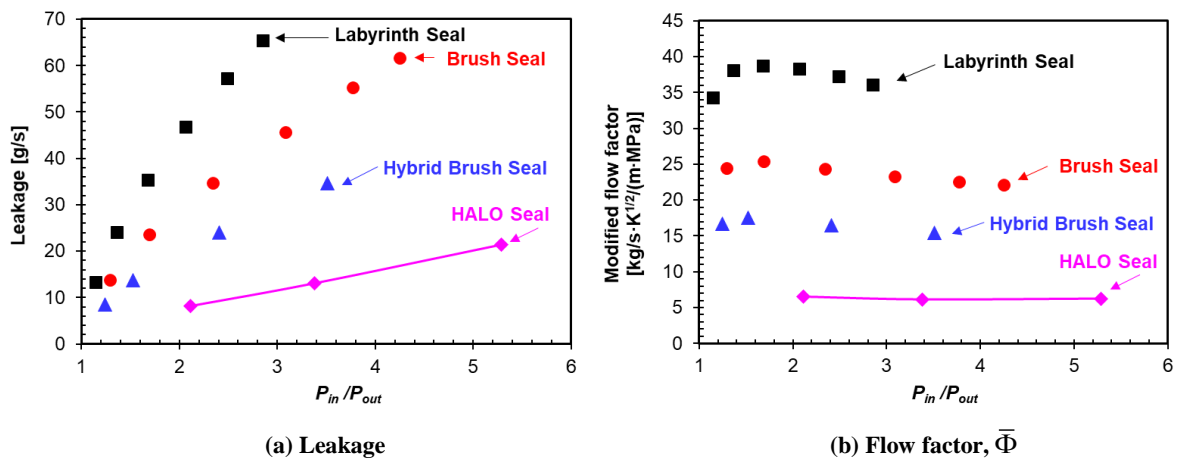


Figure 16 Photographs of four short length metal seals and schematic views of the axial thru flow [26].



|   |                                       |
|---|---------------------------------------|
| <b>Disk material</b>                      | 4140 Steel                            |
| Thermal expansion coefficient, $\alpha$   | $11.2 \cdot 10^{-6}/^{\circ}\text{C}$ |
| Disk diameter, $D$                        | 166.85 mm                             |
| Disk thickness                            | 44.45 mm                              |
| <b>Labyrinth seal material</b>            | 4140 Steel                            |
| Thermal expansion coefficient, $\alpha$   | $11.2 \cdot 10^{-6}/^{\circ}\text{C}$ |
| Seal axial length, $l$                    | 8.40 mm                               |
| Number of knives                          | 3                                     |
| Knife tip thickness                       | 0.17 mm                               |
| Pitch between knives                      | 3.5 mm                                |
| Cavity depth                              | 3.0 mm                                |
| <b>Seal clearance (<math>2C_r</math>)</b> | 0.51 mm                               |

|   |                                       |
|---|---------------------------------------|
| <b>All-metal (HALO) seal material</b>     | Inconel 718                           |
| Thermal expansion coefficient, $\alpha$   | $12.0 \cdot 10^{-6}/^{\circ}\text{C}$ |
| Outer diameter, $S_{OD}$                  | 183.05 mm                             |
| Inner diameter, $S_{ID}$ (upstream)       | 167.28 mm                             |
| Inner diameter, (downstream)              | 167.10 mm                             |
| Seal axial length                         | 8.48 mm                               |
| Pad allowable radial movement             | 0.27 mm                               |
| Pad axial length, $l$                     | 8.05 mm                               |
| Pad arc length ( $40^{\circ}$ )           | 58.42 mm                              |
| Number of pads                            | 9                                     |
| Beam axial width                          | 6.40 mm                               |
| <b>Seal clearance (<math>2C_r</math>)</b> | 0.43 mm                               |

Figure 17 Leakage and flow factor ( $\bar{\Phi}$ ) versus inlet pressure  $P_{in}$  for four (short length) seals and high temperature operation ( $300^{\circ}\text{C}$ ). Data from [25], [26].

Please refer to [25] and [26] for more details and test data on the experiments and findings. Incidentally, the HALO® seals have been applied to compressors with great success; see [29] and [30].

### Leakage for Balance Pistons – Comparison of Seal Types

Balance piston seals in multi-stage axial compressors aim to equilibrate the axial thrust. These are typically long seals that withstand large pressure differentials and can generate large reaction forces affecting the rotating system stability and dynamic forced performance.

In 2012, Ertas et al. [31] conducted measurements of leakage for four competing seal types; a labyrinth seal (LS), a honeycomb seal (HS), and two fully-partitioned pocket-damper seals (FPDS). Figure 18 displays cross-sections for each seal type. The LS and HS are 65 mm in length, and both FPDSs have a length of 102 mm. The LS has 14 knives with sharp edges and cavities' depth

equals 4 mm. The HS has cells with a depth of 2.6 mm. The eight-pocket FPDSs differ in the depth of their cavities, one is here termed shallow ( $3.17 \text{ mm} = 1/8''$ ), and the other deep ( $6.35 \text{ mm} = 1/4''$ ). The rotor diameter  $D=170 \text{ mm}$  and the radial clearance for the four seals  $C_r=0.3 \text{ mm}$  is the same.

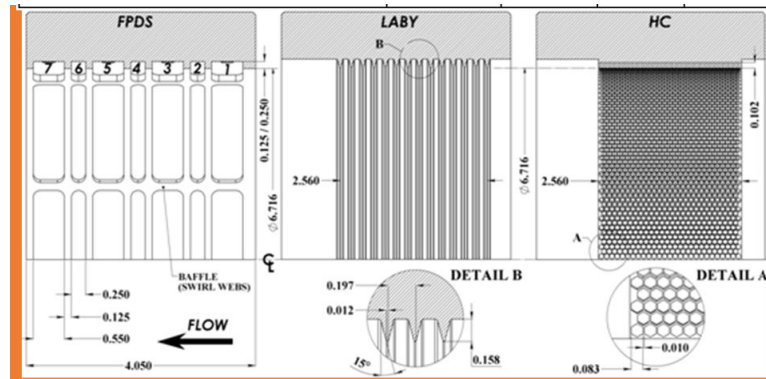


**Figure 18** Cross-section of a pocket damper seal (FPDS), a labyrinth seal (LS) and a honeycomb seal (HC) views of the axial thru flow. Taken from [31].

Figure 19 shows a comparison between the conventional PDS and a FPDS. A conventional pocket damper seals includes active and inactive segments alternating along the length of the seal. Inactive segments are continuous circumferential grooves as those in LSs (i.e. without buffer walls) and that maintain a constant pressure in the cavity during rotor whirl. Active groove segments are segregated with buffer walls. A FPDS includes buffer walls or ribs spanning the entire length of the seal, thus producing only active segments. The PDS may include notches toward the exit blade to enlarge the effective exit clearance, whereas the FPDS only has a straight through clearance.

Seal leakage measurements were conducted with air supplied at  $41.4 \text{ }^\circ\text{C}$  and an inlet (supply) pressures  $P_{in}$  ranging from 3 bar to 23 bar. The discharge pressure is ambient  $P_{out}=1.01 \text{ bar}$ . The inlet swirl velocity equals  $60 \text{ m/s}$ , and the rotor speed reached  $15 \text{ krpm}$  (surface speed= $133 \text{ m/s}$ ).

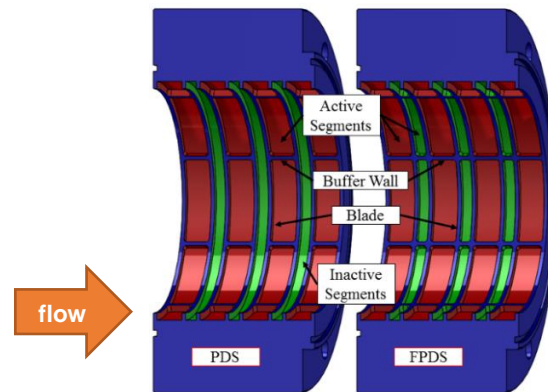


**Figure 19** Standard pocket damper seal (PDS) and fully-partitioned pocket damper seal (FPDS): similarities and differences.

Figure 20 presents the recorded flow and  $\bar{\Phi}$  vs.  $P_{in}$  for the four test seals. In dimensional form, the four seals allow approximately the same leakage, and which appears to linearly increase as the inlet pressure increases. The modified flow factor, on the other hand, reveals differences. The authors in [31] note shaft speed or inlet circumferential pre-swirl velocity did not affect the mass flow rate through the seals. The LS leaked the most, and followed by the FPDS with deep pockets ( $1/4''$ ). The HS leaked less but still more than the FPDS with shallow pockets ( $1/8''$ ). A seal effective clearance ( $=c_d C_r$ ) follows from  $\bar{\Phi}$ . As an average over the pressure range considered,  $c_d=0.32$  for the LS,  $c_d=0.318$  for the deep FPDS,  $c_d=0.304$  for the honeycomb seal, and  $c_d=0.291$  for the shallow FPDS.

Sheng et al. [32] present more measurements of leakage in various seal types and include their characterization in terms of an effective clearance, most useful to benchmark the effectiveness of brush seals.

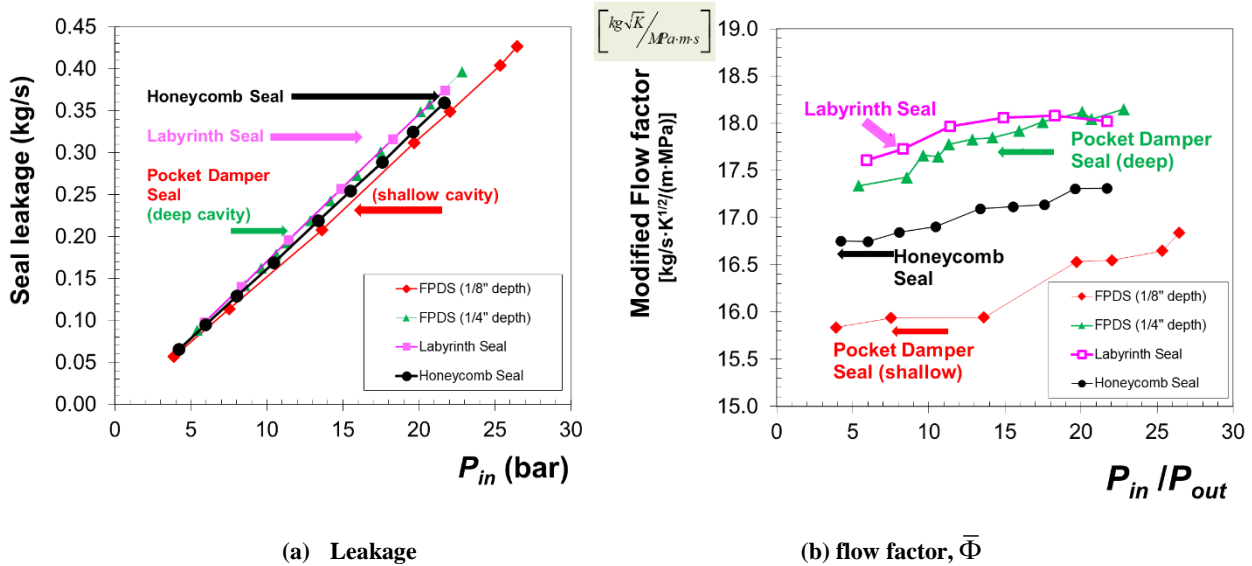


Figure 20 Leakage and flow factor ( $\bar{\Phi}$ ) versus inlet pressure ( $P_{in}$ ) for four long seals: a labyrinth seal, a honeycomb seal, and two pocket damper seals (FPDS) differing in cavity depth. Data from [31].

### Leakage for Impeller Eye Seals

Located on the outer surface of a shrouded impeller, eye seals restrict the leakage from the discharge section of the impeller into the low pressure at the inlet of the stage; see Figure 1. These seals are relatively short in length and the inlet swirl velocity likely is near the impeller surface speed at that location. That is, the inlet swirl ratio at the seal inlet plane can be larger than 0.5.

With the need to develop and to qualify multiple phase-flow for subsea submersible pumps and compressors, Torres et al. [33] recently measured the leakage of impeller eye seals operating with controlled gas/liquid mixtures. Figure 21 depicts the cut-out of a stepped clearance FPDS and a LS, both having the same axial length  $L = 48$  mm and shaft diameter  $D = 127$  mm. The steps, 6 mm wide and 0.09 mm in height, are machined on the rotor surface. The LS has 4 sharp knives and three cavities, each 4.8 mm in depth. The PDS has eight pockets, 4.8 mm in depth, around the circumference. The smallest clearance ( $C_r$ ) for the PDS equals 0.106 mm whereas that for the LS is 0.14 mm. A smooth surface rotor, one without steps, was also manufactured to render uniform clearance seals,  $C_r = 0.196$  mm for the PDS, and 0.23 mm for the LS.

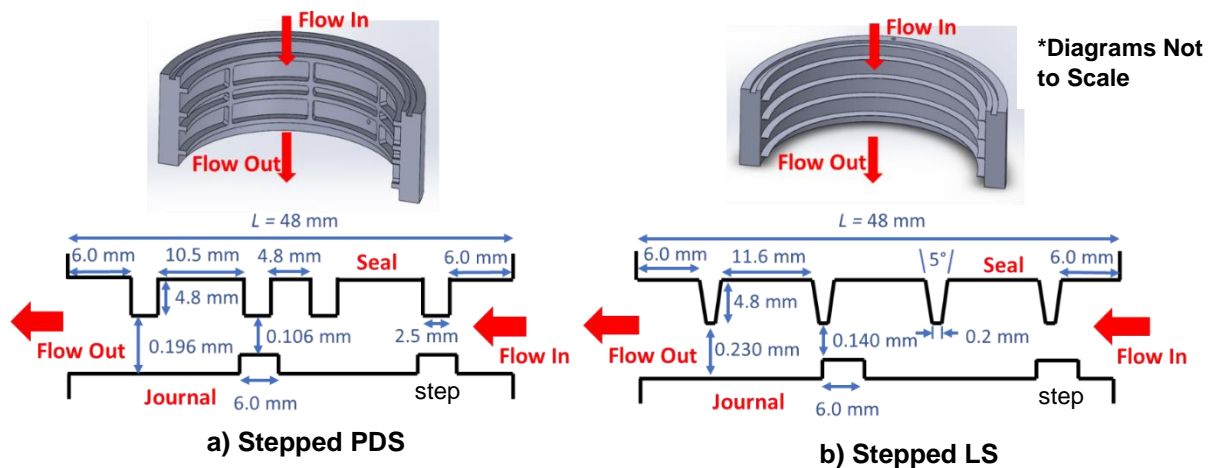
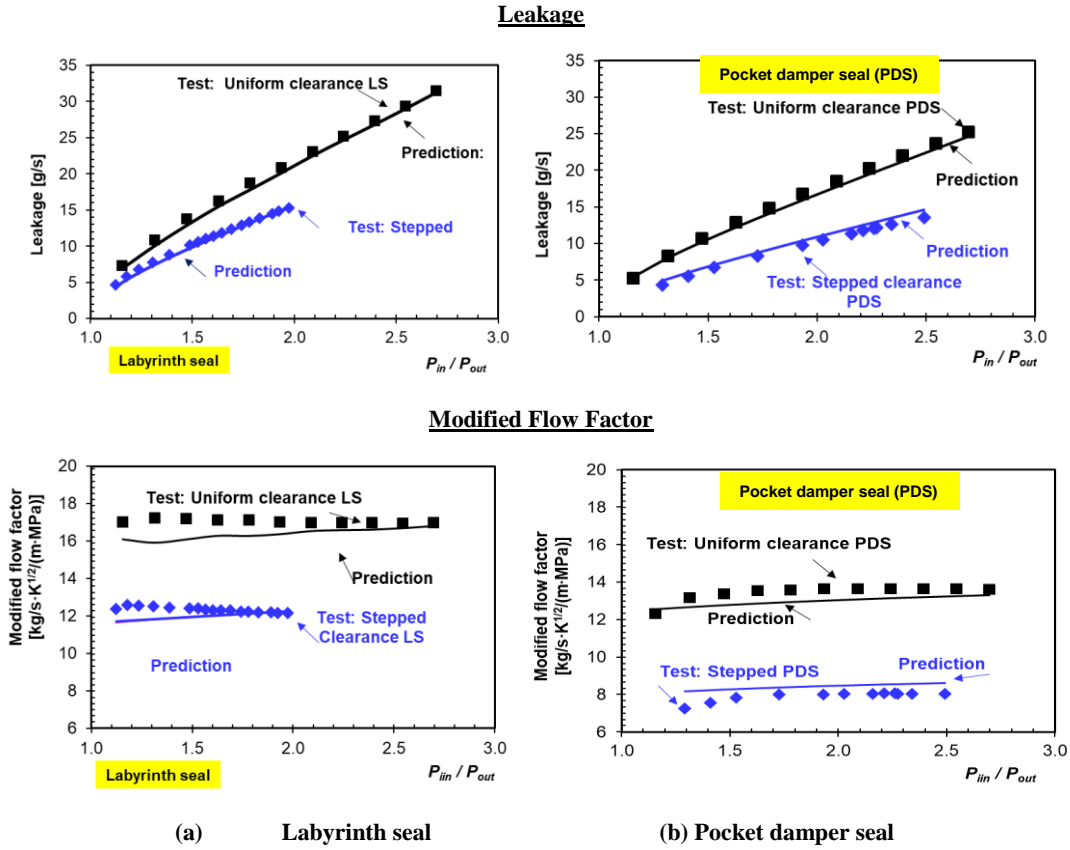


Figure 21 Cut-outs and cross-section of a stepped clearance PDS and a stepped clearance LS (not to scale). Taken from [33].

The experiments were conducted with pressurized air at room temperature (294 K) and  $P_{in} = 2.8$  bar maximum. The exit pressure is ambient  $P_{out} = 1$  bar. The rotor angular speed increased from (0 rpm), to 3 krpm, and then a top speed of 5.25 krpm (surface speed  $\sim 35$  m/s). Shaft speed was found to have negligible influence on the measured leakage.

Figure 22 presents the recorded flow and  $\bar{\Phi}$  vs. ( $P_{in}/P_{out}$ ) for the LS and PDS. Each graph contains data for the stepped clearance and uniform clearance configurations, as well as predictions from bulk-flow models. As expected, the LS leaks more than the PDS on account of its larger clearance, 0.23 mm vs. 0.196 mm, i.e., 17% higher. The stepped clearance seals leak less since their smaller clearances reduce leakage, 0.106 mm for the PD vs. 0.14 mm for the LS. The modified flow factor ( $\bar{\Phi}$ ) demonstrates the PDS, with a uniform clearance or a stepped clearance, outperforms the LS.

As the  $\bar{\Phi}$  s are nearly constant over the pressure range considered, the seals' effective clearance ( $C_e = c_d C_r$ ) is also a constant. From the derived  $\bar{\Phi}$ ,  $c_d = 0.40$  and  $0.47$  for the uniform clearance and stepped clearance labyrinth seals, respectively. Similarly,  $c_d = 0.36$  and  $0.40$  for the uniform clearance and stepped clearance PD seals, respectively. The increase in  $c_d$  for the stepped clearance seals follows from using the clearance at the step as the characteristic magnitude. Predictions of leakage ( $\bar{\Phi} \rightarrow c_d$ ) are very good for both the PDS and the LS.



**Figure 22 Leakage and flow factor ( $\bar{\Phi}$ ) versus pressure ( $P_{in}/P_{out}$ ) for a labyrinth seal (left) and a pocket damper seal (right). Comparison between uniform clearance and stepped clearance configurations. Data from [33].**

The extensive comparisons of measured and predicted seals' leakage shown above demonstrate that (well designed and engineered) annular seals have effective clearances that are a fraction of their operating clearance. The typical range is  $C_e/C_r = c_d \sim 0.30 - 0.40$ . Most importantly, for the experimental data reviewed,  $c_d$  is not a function of either the inlet pressure, or the outlet pressure, or the shaft speed, or the actual clearance! This remarkable finding attests to the well understood nature of the fluid flow through the seals. Simple bulk-flow model, and of course CFD models, predict accurately the leakage of this type of annular clearance seals.

## EFFECT OF SEALS ON ROTORDYNAMIC STABILITY

### A Summary of Seal Reaction Forces and Seal Force Coefficients

Consider as depicted in Figure 23 a rotor turning with angular speed  $\Omega$ , and its center displaces with small amplitude whirl motions ( $X(t)$ ,  $Y(t)$ ) around the center of the seal stator. The rotor motion generates a dynamic pressure field in the seal which produces a reaction force with components ( $F_x$ ,  $F_y$ ). The generally accepted force-rotor displacement model is,

$$-\begin{bmatrix} F_x \\ F_y \end{bmatrix} = \begin{bmatrix} K_{(\omega)} & k_{(\omega)} \\ -k_{(\omega)} & K_{(\omega)} \end{bmatrix} \begin{bmatrix} X \\ Y \end{bmatrix} + \begin{bmatrix} C_{(\omega)} & c_{(\omega)} \\ -c_{(\omega)} & C_{(\omega)} \end{bmatrix} \begin{bmatrix} \dot{X} \\ \dot{Y} \end{bmatrix} \quad (9)$$

Above ( $K$ ,  $k$ ) and ( $C$ ,  $c$ ) represent the mechanical element stiffness and damping force coefficients. Until the late 1990s' these coefficients were regarded as constant (frequency independent), a function of the seal geometry and the operating conditions in shaft surface speed ( $\Omega$ ) and the pressure drop ( $\Delta P$ ) across the seal [2], [3]. Note that in a turbomachine,  $\Delta P$  is typically a function of shaft speed, i.e.,  $\Delta P \sim \Omega^2$ . Fluid compressibility, characteristic of gases and supercritical fluids, leads to force coefficients that are a function of the whirl frequency ( $\omega$ ) while being modestly affected by the motion amplitude.

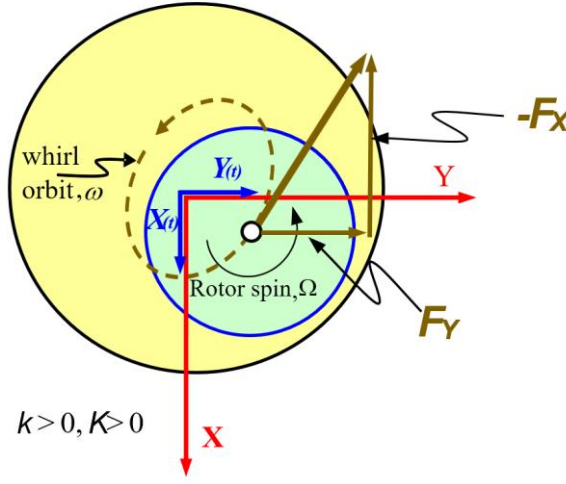


**Figure 23 Schematic view of rotor whirl motion and seal reaction forces (drawing not to scale).**

Consider circular centered orbits with amplitude  $r$  and frequency  $\omega$  then  $X(t) = r \cos(\omega t)$  and  $Y(t) = r \sin(\omega t)$ ; and Eq. (10) becomes

$$-\begin{bmatrix} F_x \\ F_y \end{bmatrix} = \left( K_{(\omega)} + \omega c_{(\omega)} \right) \begin{bmatrix} X \\ Y \end{bmatrix} + \left( C_{(\omega)} - k/\omega \right) \begin{bmatrix} \dot{X} \\ \dot{Y} \end{bmatrix} \quad (10)$$

In a moving coordinate system  $(r, t)$  turning with the same frequency, the radial and tangential components of the seal reaction force equal

$$F_r = -K_{eff(\omega)} r ; F_t = -C_{eff(\omega)} (r\omega) \quad (11)$$

$$\text{where} \quad K_{eff(\omega)} = \left( K_{(\omega)} + \omega c_{(\omega)} \right), \quad C_{eff(\omega)} = \left( C_{(\omega)} - k_{(\omega)}/\omega \right) \quad (12)$$

are the effective stiffness and effective damping coefficients. Note that  $K_{eff} > 0$  produces a centering force as the radial force  $F_r < 0$ , whereas  $C_{eff} > 0$  promotes dynamic stability since the tangential force  $F_t < 0$ . Seal configurations that produce a significant effective damping coefficient are desirable, and those that do not generate a cross-coupled stiffness ( $k = 0$ ) are best. Note that the cross-coupled damping coefficient  $c_{(\omega)}$  when positive aids to increase the centering stiffness of the seal.

In annular seals, the fluid inlet swirl (circumferential) velocity affects the seal dynamic force performance, in particular the cross-coupled stiffnesses ( $k$ ). That is, moving through the seal, the fluid (gas) swirls as it is dragged by the rotor surface with speed  $U_s = \frac{1}{2}D\Omega$ . After travelling through the seal, the fluid exits with an average circumferential speed  $U_e \rightarrow \frac{1}{2}U_s$ .

A whirl frequency ratio (WFR) is defined as

$$WFR = \frac{k}{C\omega} \quad (13)$$

and the effective damping can be written as

$$C_{eff(\omega)} = C_{(\omega)} (1 - WFR) \quad (14)$$

Clearly, as the  $WFR$  grows, the effective damping decreases.

In a seal where hydrodynamic effects dominate (circumferential flow  $\gg$  axial flow),  $k \sim (\frac{1}{2}\Omega C)$ ; that is, the cross-stiffness ( $k$ ) grows with the shaft angular speed ( $\Omega$ ). For rotor motions due to a rotating imbalance, the rotor whirl is synchronous with shaft speed,  $\omega = \Omega$ , and a  $WFR = 0.50$  follows. Note that for this condition,

$$C_{eff(\omega=\Omega)} = C \left( 1 - \frac{1}{2} \right) = \frac{1}{2} C \quad (15)$$

That is, for operation with  $\omega = \Omega$ , the seal damping is effectively 50% less (lower).

Now, consider the whirl frequency ( $\omega$ ) equals a system natural frequency ( $\omega_n$ ). Hence, shaft whirl motions at this frequency produce an effective damping coefficient

$$C_{eff(\omega_n)} = C \left( 1 - \frac{\Omega}{2\omega_n} \right) \quad (16)$$

and note that  $C_{eff(\omega_n)} \leq 0$  for  $\Omega \geq 2\omega_n$ . This relation dictates the maximum shaft speed ( $\Omega_{max}$ ) the system can operate for the mechanical element (and presumably the whole rotor bearing system) to be stable. That is, with  $WFR = \frac{1}{2}$ , the shaft speed is at most twice as large as the system natural frequency.

From Eq. (12),

$$C_{eff}(\omega_{break}) = 0 \rightarrow \omega_{cross-over} = \left( \frac{k}{C} \right) \quad (17)$$

When characterizing a seal, the frequency at which  $C_{eff} \sim 0$  is important. This frequency is termed as a *cross-over frequency*.

A **swirl brake (SB)** formed by a series of uniformly distributed vanes around a circumference is a common mechanical element that reduces the circumferential velocity before its ingress into the seal, hence enhancing the stability of a rotor-bearing system. Figure 24 depicts a typical SB for installation upstream of a labyrinth seal. Note that SBs efficiency reduces as the rotor speed increases since the circumferential flow is larger than the axial flow. Figure 25 shows two honeycomb seals with SBs, one having axial vanes and the other with vanes angled against shaft rotation. Clearly, the last configuration will reduce *more* the generation of a *destabilizing k* since the vanes not just retard but also intend to reverse the direction of the swirl flow into the seal inlet.

Presently, balance piston seals, i.e. long seals, are currently implemented with swirl brakes (SBs). Not doing so could be deleterious to the stability of the system as too many incidents attest to costly, often catastrophic failures [3], [11], [34].

References [35], [36] present details on the design and optimization of swirl brakes with due account to geometry and operating characteristics. It is important to emphasize that the effectiveness of SBs reduces as the shaft speed increases (above the intended design condition). In general, SBs do not affect the leakage of the downstream annular seal element.

This last condition may not occur in impeller eye seals since they are short in a very confined space. The addition of a SB will likely remove one of the knives in the LS making it less effective to restrict leakage; see Figure 26. On the other hand, a SB at this location, downstream of the impeller discharge, is rather beneficial to the rotor system dynamics, as demonstrated in [37].

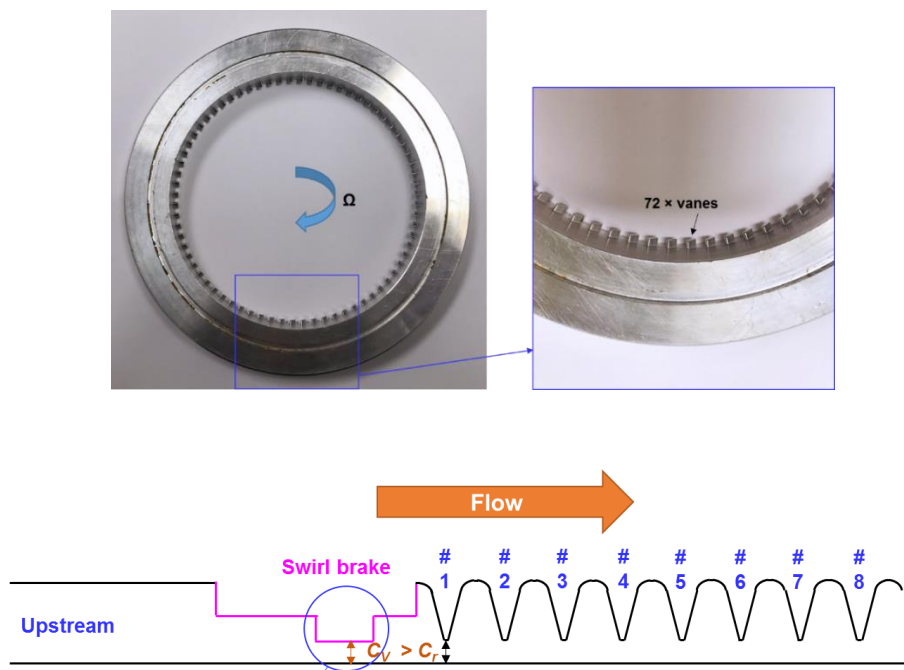


Figure 24 Photographs of a swirl brake (SB) with 72 vanes and stagger angle  $\theta = 50^\circ$  (against shaft rotation) and illustration of its location upstream of a LS.

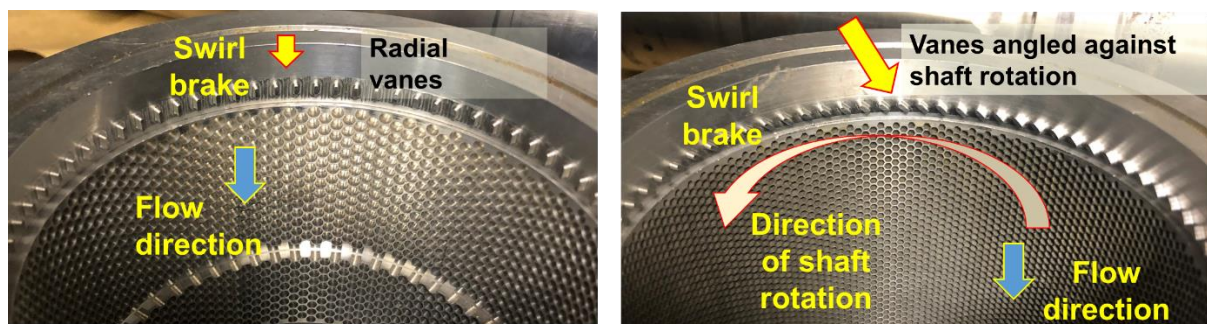
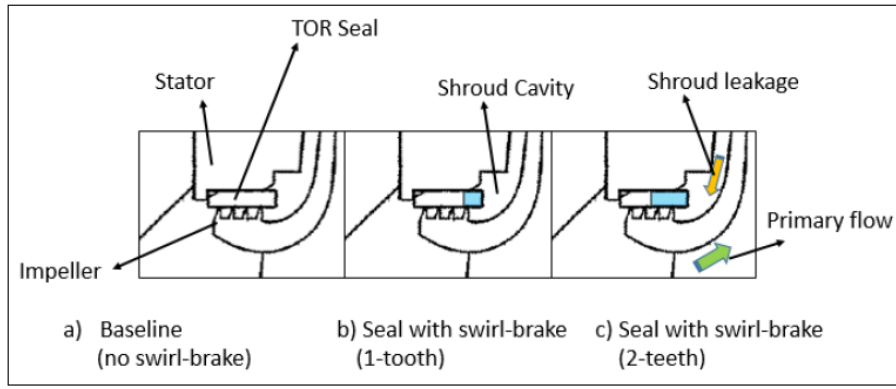


Figure 25 Photographs of honeycomb seals with swirl brakes (radial and angled vanes).



**Figure 26 Knives on rotor (TO) impeller eye seal: baseline and modified with a swirl brake. Reproduced with permission from [37].**

### Numerical Evaluation of Seal Force Coefficients

The literature producing experimentally obtained (and predicted) seal force coefficients is quite extensive. Childs and Vance [11] (1997) and Childs [34] (2013) give detailed accounts of the influence of seal forces on the rotordynamics of turbomachinery. Presently textured surface seals (damper seals) offer a remarkable opportunity to tailor the rotordynamic performance and stability of turbomachinery. There are many engineered seal types that offer both leakage control and aid to rotordynamic stability.

Prediction models for seal force coefficients, namely stiffness and damping, abound. One must remember that the said force coefficients represent reaction forces for infinitesimally small amplitude motions about an equilibrium condition. For seals, the centered condition is selected as these elements are typically designed not to carry a static load. Hence, the models assume the shaft or rotor describes whirl motions with a certain amplitude  $(\Delta e_x, \Delta e_y) \ll C_r$  and frequency  $(\omega)$ . The shaft dynamic displacements modify the seal radial gap that becomes  $h = C_r + [\Delta e_x \cos \theta + \Delta e_y \sin \theta] e^{i\omega t}$ , and then the pressure field is  $P = P_0 + [\Delta e_x P_x + \Delta e_y P_y] e^{i\omega t}$ . Here,  $P_0$  represents the equilibrium pressure field, and  $(P_x, P_y)$  are dynamic components of pressure.

In a bulk flow model (BFM), both the film gap  $(h)$  and pressure  $(P)$  are substituted into the fluid mass conservation and momentum transport equations to obtain zeroth order (equilibrium flow) and first order ordinary differential equations for the evaluation of  $P_0$  and  $(P_x, P_y)$ . Setting physically correct boundary conditions at the seal inlet and outlet planes close the problem and permit a unique solution. The force coefficients follow from integration of the dynamic pressures on the rotor surface

$$\begin{bmatrix} K_{XX} + i\omega C_{XX} & K_{XY} + i\omega C_{XY} \\ K_{YX} + i\omega C_{YX} & K_{YY} + i\omega C_{YY} \end{bmatrix} = \iint [P_x \quad P_y]_{(\omega)} \begin{bmatrix} \cos \theta \\ \sin \theta \end{bmatrix} R d\theta dz \quad (18)$$

Above, for an axisymmetric seal,  $K = K_{XX} = K_{YY}$ ,  $C = C_{XX} = C_{YY}$ ,  $k = K_{XY} = -K_{YX}$ ,  $c = C_{XY} = -C_{YX}$ .

CFD models on the other hand must solve for the whole flow field considering finite displacements of the shaft center. If the seal is axisymmetric, a clever transformation with a moving coordinate system attached to the whirling rotor allows the flow to appear steady in the rotating frame. For other seal types, shaft dynamic displacements, single or multiple frequency, are specified and the *solver* proceeds to find the time-transient solution of the flow equations until a measure of convergence is achieved.

The computational process is long and tedious with much attention given to the ability of the mesh to deform and to follow the shaft displacements. Integration of the (calculated) pressure field on the rotor surface produces the seal reaction forces  $(F_x, F_y)$ , and from which the force coefficients follow by curve fitting using the whirl frequency  $(\omega)$  as the independent parameter. For example, for a circular orbit with  $X_{(t)} = r \cos(\omega t)$  and  $Y_{(t)} = r \sin(\omega t)$ ; note that at  $t=0$  or  $2\pi/\omega$ ,  $X = r$  and  $Y = 0$ , whereas  $\dot{X} = 0$  and  $\dot{Y} = r\omega$ . Hence, from Eq (11)

$$-\frac{F_{x(\omega)}}{r} \rightarrow (K_{(\omega)} + \omega c_{(\omega)}); \quad -\frac{F_{y(\omega)}}{r\omega} \rightarrow (C_{(\omega)} - k/\omega) \quad \text{at } t=0 \quad (19)$$

Experimentally, seal force coefficients are obtained in dedicated (ad-hoc) test rigs with abundant instrumentation to record forces and shaft displacements. The most successful type of rig is one that *floats* or soft mounts the test element on a rotating rigid shaft. Initially conceived by Glienicke [38], this type of simple test rig includes external loaders (typically shakers or impactors) to excite the seal or bearing housing and then recording its ensuing acceleration and displacement relative to the spinning shaft. Two independent load excitations, along the lateral directions  $X$  and  $Y$  and at a prescribed set of whirl frequencies, provide enough information to identify experimentally the seal force coefficients. One must note that the element force coefficients shown in the literature are valid over a certain frequency range. The method is well known and detailed in multiple publications; for example Ref. [39].

In the following, seal stiffness and damping force coefficients, experimental and predicted, are shown in dimensionless form. The parameters of importance are the pressure drop across the seal  $(P_{in} - P_{out})$ , its length  $(L)$ , diameter  $(D)$ , and operating clearance  $(C_r)$ , and the shaft operating speed  $(\Omega)$ . The dimensionless coefficients are defined as

$$\begin{aligned} (K^* \quad k^*) &= (K \quad k) \frac{C_r}{(P_{in} - P_{out})LD} \\ (C^* \quad c^*) &= (C \quad c) \frac{C_r \Omega}{(P_{in} - P_{out})LD} \end{aligned} \quad (20)$$

### Comparison of Force Coefficients for Various Seal Types: Experimental Results and Predictions

Over the last 30 years, the published literature shows dozens of papers and technical reports presenting experimental force coefficients for gas seals. A much larger body of publications also presents model predictions and comparisons to the published experimental results. At the onset of the 21<sup>st</sup> century, bulk flow models (BFM) were the state of the art. Presently, CFD tools and models are common place in routine engineering work.

#### Force coefficients for a honeycomb seal vs. a smooth seal vs. a labyrinth seal

Only a few references purposely compare force coefficients for one seal type vis-a-vis other seal type. Childs et al. [40] were first to benchmark honeycomb seals (HS) against a smooth surface annular seal and a labyrinth seal (LS). The three seals have the same rotor diameter ( $D = 152$  mm), length ( $L/D = 1/3$ ), rotor and radial clearance ( $C_r = 0.41$  mm). Childs et al. first tested seven HSs whose cell depth and size varied while operating with shaft speed up to 16 krpm (127 m/s surface speed) and inlet to exit pressure ratios ranging from 3.03 to 8.0

| $L/D = 1/3$             | HS #7 | LS   |
|-------------------------|-------|------|
|                         | mm    | mm   |
| Radial clearance, $C_r$ | 0.41  | 0.41 |
| Cavity/Cell width       | 1.57  | 3.2  |
| Cavity/Cell depth       | 1.91  | 3.2  |
| Number of blades        | N/A   | 16   |

Figure 27 depicts the three seals' cross-coupled stiffness ( $k^*$ ) and direct damping ( $C^*$ ) coefficients vs. shaft speed for operation with  $P_{in}/P_{out}=3.08$  and no gas pre-swirl rotation. The smooth surface seal has the largest  $k$ , and increasing with shaft speed. Same for the HS that has a negative  $k$  for shaft speeds below 10 krpm (8 m/s surface speed). The LS shows  $k < 0$ , contrary to common expectation. Note the HS has the largest damping,  $C^*$  increases with shaft speed. The LS offers a small damping though also increasing with shaft speed.

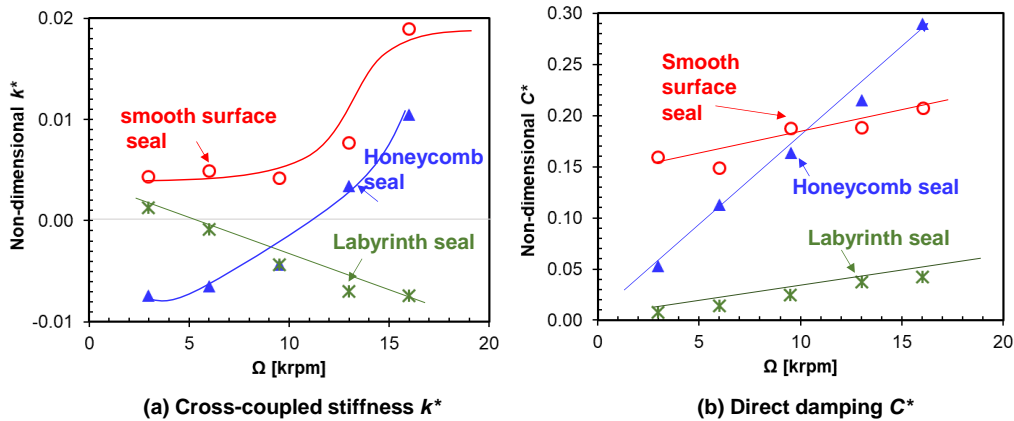


**Figure 27 Comparison of cross-coupled stiffness and damping coefficients vs. shaft speed for three seals: a labyrinth seal, a honeycomb seal, and a smooth surface seal.  $P_{in} = 3.08$  bar,  $P_{out} = 1$  bar. Null pre-swirl velocity. Experimental data from [40].**

The whirl frequency ratio,  $WFR = k/(C\Omega)$ , shown in Figure 28, for most inlet circumferential swirl flow speeds, favors the honeycomb seal as the most stabilizing mechanical element,  $WFR \sim 0$ . However, the LS shows a negative  $WFR$  for fluid inlet pre swirl opposing shaft rotation. In any case, the smooth surface seal has the largest  $WFR$  which equals 1.0 for an inlet pre-swirl as large as the surface speed of the rotor.

Note that at the time (1989), force coefficients for gas seals were not regarded as frequency dependent. That view changed by the end of the 1990s when more experimental results and theoretical developments made evident the frequency dependency of gas seal force coefficients.

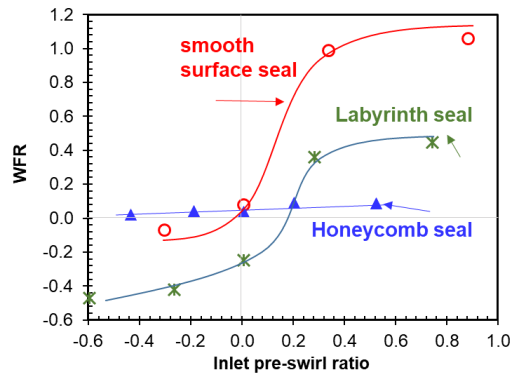


Figure 28 Whirl frequency vs. inlet circumferential flow for a labyrinth seal, a honeycomb seal, and a smooth surface seal.  $P_{in} = 8.28$  bar,  $P_{out} = 1$  bar. Rotor speed = 16 krpm (surface speed = 35 m/s). Experimental data from [40].

### Force coefficients for a balance piston seal (moderate pressures) – comparison of seal types

Ertas et al. [31] compare the rotordynamic force coefficients for a labyrinth seal (LS), a honeycomb seal (HS), and a fully-partitioned pocket-damper seal (FPDS) with shallow cavity depth ( $1/8''$ ). The rotor diameter  $D$  equals 170 mm, and the radial clearance  $C_r = 0.3$  mm is the same for the three seals. The reference produces experimental force coefficients for operation at two rotor speeds (7 and 15 krpm), pressure drops as large as 6.9 bar, and under two inlet swirl conditions. Figure 20 shows the leakage for the three seals.

| Diameter=170 mm         | FPDS     | HS   | LS  |
|-------------------------|----------|------|-----|
|                         | mm       | mm   | mm  |
| Seal length, $L$        | 102      | 65   | 65  |
| Radial clearance, $C_r$ | 0.3      | 0.3  | 0.3 |
| Cavity/Cell width       | 13.3/5.7 | 0.79 | 4.3 |
| Cavity/Cell depth       | 3.1      | 3.2  | 4.3 |
| Number of blades        | 8        | N/A  | 20  |

Figure 29 depicts the seals' force coefficients vs. the excitation frequency ratio ( $\omega/\Omega$ ) for operation at 15 krpm and pressure ratio  $P_{in}/P_{out}=6.9$ . The inlet swirl speed = 0 m/s whereas the rotor surface speed = 133.5 m/s. The experimental results show the coefficients are strong functions of the excitation frequency. Note that  $\omega/\Omega=1$  is a synchronous whirl excitation. The LS with knives on the stator offers the smallest  $k$ ,  $C$  and  $C_{eff}$ . The HS produces a significant direct stiffness ( $K$ ) while the FPDS shows  $K$  ranging from negative to positive as the frequency increases,  $\omega > 1/2 \Omega$ . Both the HS and FPDS produce about the same cross-coupled stiffnesses ( $k$ ), and which decrease as the frequency increases. Notably, the HS and the FPDS produce nearly five and six times more direct damping than the LS does. Similarly,  $C_{eff}$ 's for the HS and the FPDS are ~ four and five times larger than the LS'  $C_{eff}$ .

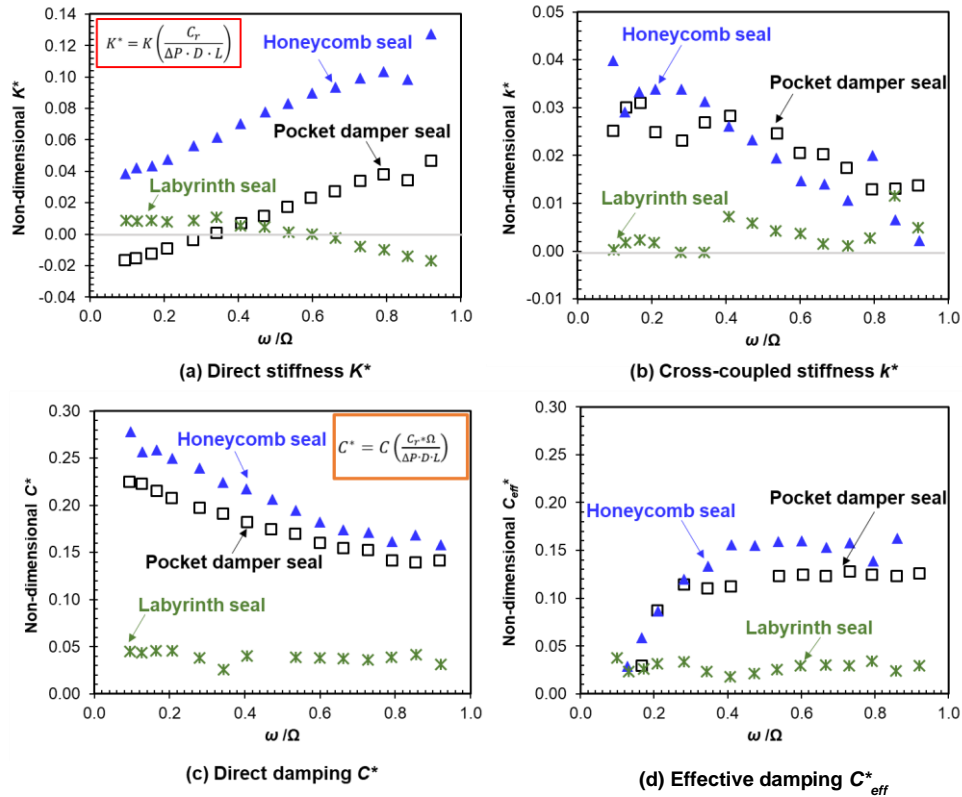
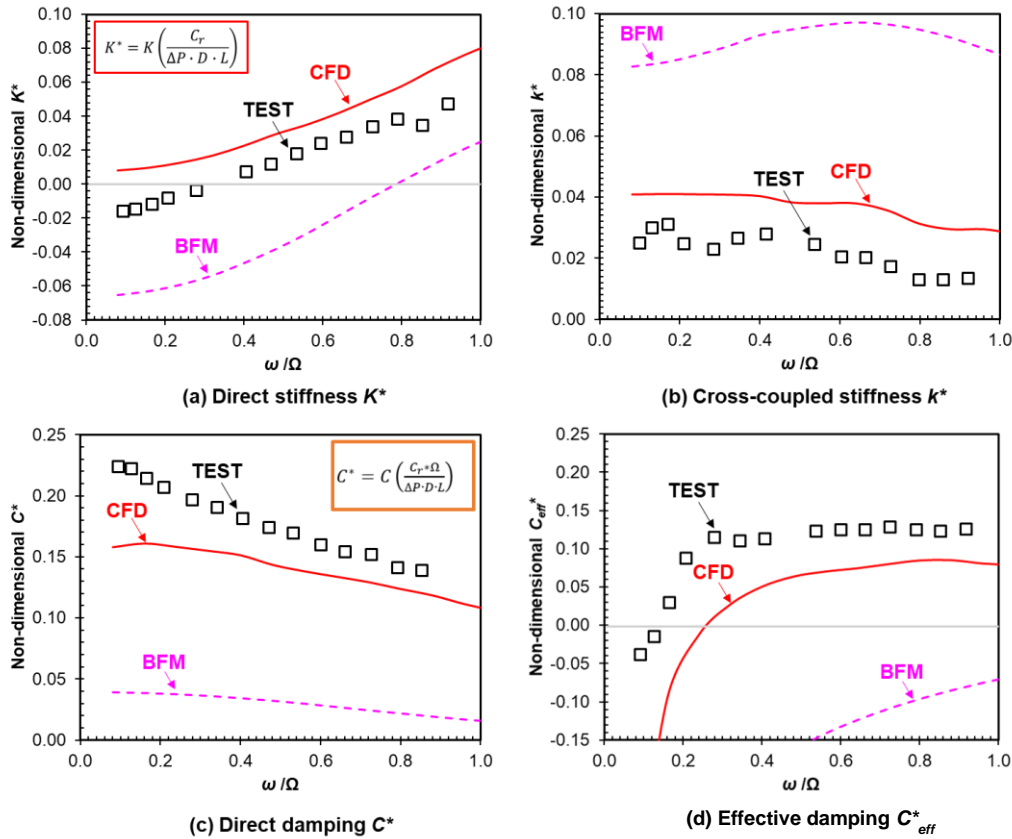


Figure 29 Comparison of experimental force coefficients for three seals: a labyrinth seal, a honeycomb seal, and a fully-partitioned pocket damper seal. (a,b) Direct and cross-coupled stiffnesses, (c) direct damping, and (d) effective damping.  $P_{in} = 6.9$  bar,  $P_{out} = 1$  bar, rotor speed = 15 krpm (surface speed = 133 m/s), null inlet swirl. Experimental data from [31].

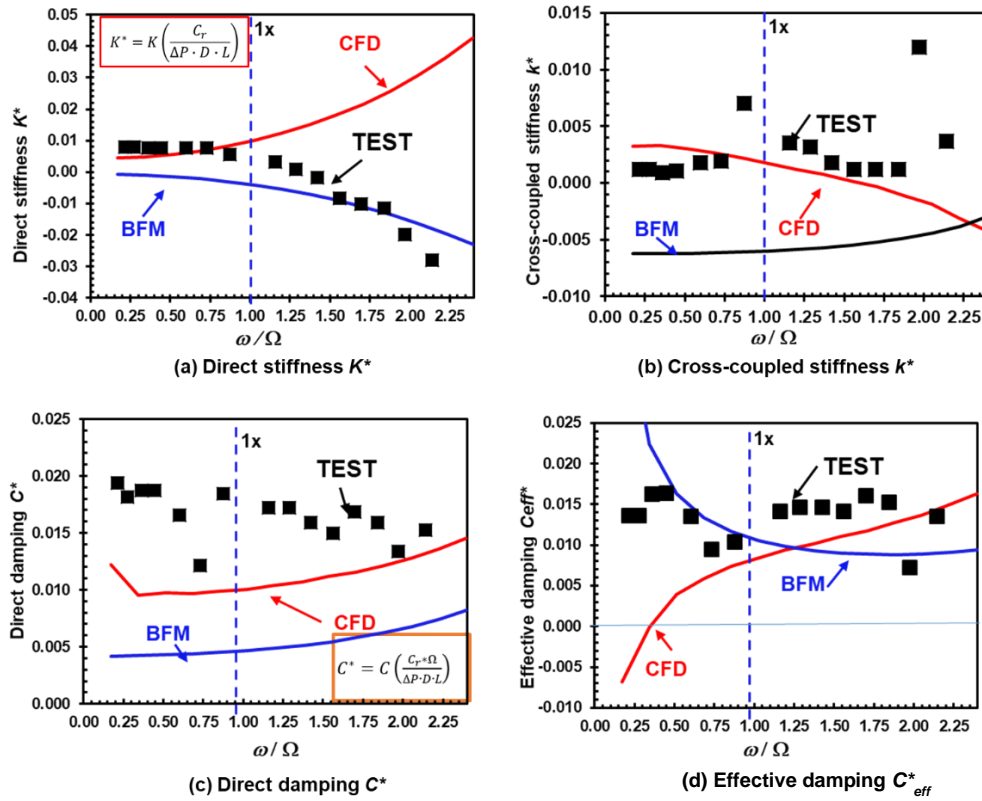
The experimental results evidence the notable damping produced by the damper seals, whether a FPDS or a HS. Importantly enough, the large direct stiffness ( $K$ ) of the HS makes it a suitable mechanical element that can share the static load in a (say) back to back centrifugal compressor. The significant  $K$  and  $C$  are a remarkable engineering achievement since presently a balance drum at the mid-span of a back to back compressor, see Figure 3, can be thought as a third bearing in a rotor-bearing system.

Figure 30 depicts the force coefficients for the FPDS and comparisons against predictions derived from a BFM [41] and a CFD model [42]. In general, the bulk-flow model predictions are not accurate, even though they produce similar trends as the experimental  $K$  and  $C$ . Predictions from the CFD model agree much better with the experimental force coefficients, in particular the cross-coupled stiffness ( $k^*$ ) and the effective damping ( $C_{eff}$ ).



**Figure 30 FPDS: experimental force coefficients vs. BFM and CFD model predictions. (a, b) Direct and cross-coupled stiffnesses, (c) direct damping, and (d) effective damping coefficients.  $P_{in} = 6.9$  bar,  $P_{out} = 1$  bar, rotor speed = 15 krpm (surface speed = 133 m/s), null inlet swirl. Experimental data in [31], CFD predictions in [42].**

For completeness, Figure 31 depicts the rotordynamic force coefficients for just the labyrinth seal (LS) vs. the whirl frequency/shaft speed ( $\omega/\Omega$ ). The graphs depict the test data acquired at shaft speed = 7 krpm [31] vs. CFD and BFM predictions reported in [43]. The BFM computational program is from [44]. Note that compared to the FPDSs or the HS, the LS offers very small effective damping ( $C_{eff}$ ) and centering stiffness ( $K$ ). In general, the CFD prediction is good for the cross-coupled stiffness ( $k^*$ ) but are well off the mark, magnitude and trend, for the direct stiffness ( $K^*$ ), in particular at high excitation frequencies. The BFM predicts more accurately  $K^*$  but does poorly for  $k^*$  ( $<0$ ) which has a different sign than the experimental result. Both the CFD and BFM results under predict the seal direct damping ( $C^*$ ); the BFM delivering the worst results. The experimental effective damping coefficient  $C_{eff} > 0$  for all whirl frequencies, while the CFD and BFM only show agreement with the test result for high frequencies,  $\omega > 1.2 \Omega$ . The trend of the CFD and BFM results at low frequencies ( $\omega \rightarrow 0$ ) are opposite. The large inlet/exit pressure ratio (6.9) evidences Ertas et al. LS operated choked, and hence, its force coefficients are not representative of most operating conditions.



**Figure 31 Labyrinth Seal: experimental force coefficients vs. BFM and CFD model predictions. (a, b) Direct and cross-coupled stiffnesses, (c) direct damping, and (d) effective damping coefficients.  $P_{in} = 6.9$  bar,  $P_{out} = 1$  bar, rotor speed = 7 krpm (surface speed = 63 m/s), 7 m/s inlet swirl. Experimental data in [31], CFD and BFM predictions in [43].**

### Force coefficients for a balance piston seal (high-pressure) – comparison of seal types

Delgado et al. [45] also conducted experiments to measure the force coefficients of a FPDS and produced comparisons against earlier data collected for a honeycomb seal (HS) and a labyrinth seal (LS). The FPDS, 115 mm in diameter  $\times$  86 mm in length ( $L/D=0.75$ ), operated at three shaft speeds (10, 15 and 20 krpm; max surface speed of 120 m/s), with supply pressure  $P_{in} = 70$  bar(a), three inlet/exit pressure ratios ( $P_{in}/P_{out}=4, 2, 1.53$ ), and with circumferential inlet flow pre-swirl conditions ranging from 10% to 160% of shaft surface speed. The FPDS has radial clearance  $C_r=0.203$  mm and features seven rows, each having eight pockets with arc length of  $43^\circ$ . Dimensions for the other two seals are in the inset table. The tests are unique since the exit pressure of the seals was controlled by side labyrinth seals and throttling the large chambers on the discharge sections.

| $L/D=0.75$              | FPDS     | HS    | LS    |
|-------------------------|----------|-------|-------|
|                         | mm       | mm    | mm    |
| Seal Diameter, $D$      | 115.1    | 114.7 | 114.7 |
| Radial clearance, $C_r$ | 0.203    | 0.200 | 0.200 |
| Cavity/Cell width       | 13.3/5.7 | 0.79  | 4.3   |
| Cavity/Cell depth       | 3.6      | 3.2   | 4.3   |
| Number of blades        | 8        | N/A   | 20    |

Delgado et al. [45] present the flow factor ( $\bar{\Phi}$ ) vs. pressure ratio ( $PR$ ) for the three test seals. The measured leakage varied little with shaft speed; and  $\bar{\Phi}$  appears to be independent of  $PR$ . From the results shown, unique loss coefficients ( $c_d$ ) for the three seals follow as:  $c_{d_{FPDS}} \sim 0.30 > c_{d_{LS}} \sim 0.25 > c_{d_{HS}} \sim 0.22$ . That is, the HS leaks the least, whereas the FPDS leaks the most. CFD model predictions for the FPDS reproduce the same  $c_d$  as the one measured.

Figure 32 shows a comparison of the direct and cross-coupled stiffnesses, direct damping and effective damping coefficients for the three seal types having the same diameter, axial length and radial clearance. As with the prior seal case, the LS offers negligible force coefficients compared to those of the HS and FPDS. The HS produces the largest direct stiffness and damping coefficients. Note  $K$  grows (hardens) with frequency while  $C$  steadily decreases. The cross-coupled stiffness is largest for the HS and decreases as  $\omega$  grows. The FPDS shows  $k$ 's as small as the ones the LS produces, and without a significant variation in frequency. The HS produces the largest effective damping coefficient for whirl frequencies lower than shaft speed. On the other hand, the FPDS has the largest  $C_{eff}$  for  $\omega > \Omega$ . Incidentally, note the cross-over frequency ( $\omega_{cross-over}/\Omega$ )  $\sim 0.10$ , a rather low magnitude, for both the HS and FPDS.

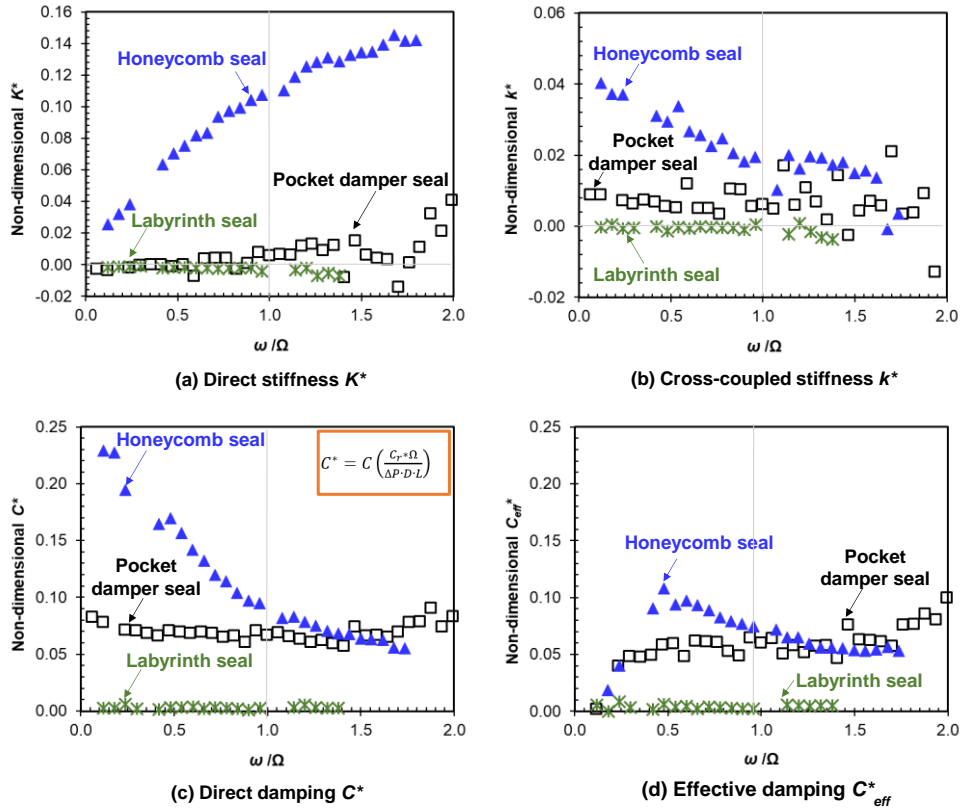


Figure 32 Comparison of force coefficients for three seals: (a, b) Direct and cross-coupled stiffnesses, (c) direct damping, and (d) effective damping.  $P_{in} = 70$  bar,  $P_{out} = 1/2 P_{in}$ , rotor speed = 10 krpm (surface speed = 60 m/s). Experimental data from [45] for low inlet pre-swirl velocity ratio.

As per comparisons to BFM and CFD model predictions obtained for the tested FPDS, Figure 33 depicts the direct and cross-coupled force coefficients vs. excitation frequency. Note the CFD predictions for both damping and effective damping follow closely the experimental results. Also the two-control volume BFM predictions [13] overpredict both  $C$  and  $C_{eff}$  while producing accurate results for the stiffnesses,  $K$  and  $k$ .

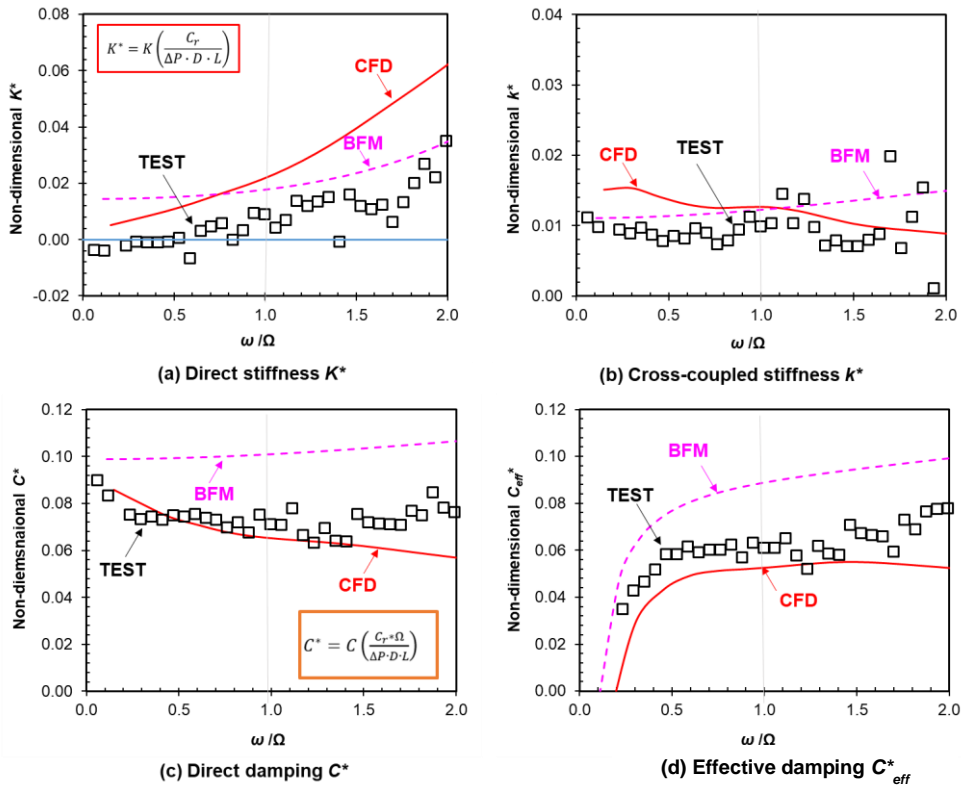


Figure 33 FPDS: experimental force coefficients vs. BFM and CFD model predictions. (a,b) Direct and cross-coupled stiffnesses, (c) direct damping, and (d) effective.  $P_{in} = 70$  bar,  $P_{out} = 1/2 P_{in}$ , rotor speed = 10 krpm (surface speed = 60 m/s). Test data from [45] for a low inlet pre-swirl velocity.

Hence, BFM predictions of force coefficients for FPDSs, see Figs. Figure 30 and Figure 33, either from the model of [41] or the model of [13], demonstrate the need to use CFD as the predictive tool. A more insightful and accurate BFM is urgently needed.

### Effective damping coefficient for impeller eye seals: a LS vs. a PDS

Figure 22 presents the leakage and modified flow factor for two impeller eye seals, one is a LS and the other is a FPDS ( $L/D = 0.38$ ). Tested by [33], the seals configurations have a uniform clearance with  $C_r = 0.196$  mm for the FPDS and  $C_r = 0.23$  mm for the LS, as can be seen in Figure 21. Both seals have four knives (3 cavities) and the damper seal has eight pockets.

Dynamic load experiments were conducted with pressurized air at room temperature (294 K) and with  $P_{in}/P_{out} = 2.71$ . The shaft maximum speed  $\Omega = 5.25$  krpm (surface speed  $\sim 35$  m/s). Figure 34 depicts the dimensionless stiffness and damping coefficients,  $K^*$  and  $C^*$ , vs. frequency ratio ( $\omega/\Omega$ ). Note the FPDS offers significantly larger stiffness and damping coefficients than the LS does, hence demonstrating the major advantage of the damper seal.

Note that the physical magnitude of the force coefficients is small (with respect to the coefficients of the test rig support structure), and the identification procedure could not provide reliable cross-coupled stiffness coefficients. Nonetheless, the results in Figure 34 show the outstanding performance of the FPDS, and including a smaller effective clearance.

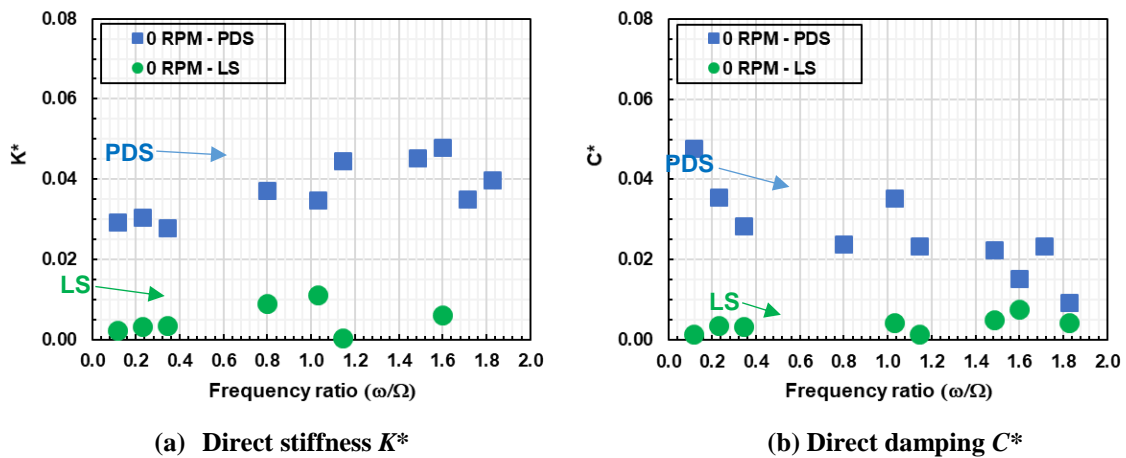


**Figure 34 Direct stiffness and damping coefficients for a uniform clearance labyrinth seal (LS) and a full-pocket damper seal (FPDS) vs. frequency. Both seals with uniform clearance, see Figure 20. Data from [33].**

The extensive comparison of dynamic force coefficients for various gas seals types makes evident that labyrinth seals (LS) produce direct stiffness ( $K$ ) and damping ( $C$ ,  $C_{eff}$ ) coefficients of small magnitude compared to those available from damper seals: honeycomb seals and pocket damper seals.

The dimensionless physical parameters are adequately characterized by Eq. (19). In particular note that at  $\omega/\Omega \sim 1$  (whirl synchronous with shaft speed), a good (reliable) estimation of the direct stiffness and effective damping for damper seals, HS and FPDS, is with  $K^*$  and  $C_{eff}^*$  in the vicinity of 0.1

$$K \sim [0.05 \rightarrow 0.10] \frac{(P_{in} - P_{out})LD}{C_r}; C_{eff} \sim [0.04 \rightarrow 0.12] \frac{(P_{in} - P_{out})LD}{C_r\Omega} \quad (21)$$

The low end of the formulas above applies to short length seals such as those in impeller shrouds, for example.

Please note that a liquid (incompressible fluid) seal with uniform clearance produces a direct stiffness and effective damping coefficients varying as [2]

$$K \sim [0.20 \rightarrow 0.40] \frac{(P_{in} - P_{out})LD}{C_r}; C_{eff} \sim [0.04 \rightarrow 0.08] \frac{(P_{in} - P_{out})LD}{C_r\Omega} \quad (22)$$

For the effective damping coefficient, the low and high ends in the range above correspond to inlet swirl ratio  $\alpha = 1/2$  and 0 (null) respectively.

## CLOSURE

Demand for high power density turbomachinery continues to drive the need to accommodate higher pressures and shaft speeds while ensuring a rotor stable operation with acceptable vibration levels. Annular clearance seals play a pivotal role on both the aerodynamic and rotordynamic performance of modern turbomachinery.

The tutorial reviews the leakage (measured and predicted) for various gas seal types versus pressure drop and versus shaft speed. The seals with a nominal clearance ( $C_r$ ) include labyrinth seals (LS) and interlocking labyrinth seals (ILS), damper seals such as

honeycomb seals (HS), pocket damper seals (PDS), conventional and hybrid brush seals, and the advanced (clearance control) HALO® seal. A flow factor characterizes the seals as a single-knife (restriction) element with an effective clearance ( $C_e$ ). The extensive comparisons of leakage, measured and predicted, reveal that engineered seals have an effective clearance  $C_e/C_r = c_d = 0.30 - 0.40$ , and which is not a function of either the inlet pressure, the outlet pressure, rotor speed, or actual clearance. The finding attests to the well-understood nature of the fluid flow through the seals. Both bulk-flow and CFD models predict accurately the leakage of most annular clearance seals, including HSs.

This tutorial also reviews the stiffness and damping force coefficients for various seal types including uniform clearance (smooth surface) seals, LS, HS, and PDS. The review of the experimental record is exhaustive with most developments on damper seals appearing in the last ¼ century. Note that LSs with teeth on the rotating surface are notorious for producing large magnitude cross-coupled stiffnesses ( $k$ ); hence, LSs are the worst as per promoting stability in a turbomachine, and not recommended for use in 21<sup>st</sup> century machinery. On the other hand, teeth on stator LS develop much smaller  $k$ , albeit not entirely free of producing a negative effective damping coefficient ( $C_{eff} < 0$ ). Poorly designed LS, acting as either balance piston seals or impeller eye seals, are the cause of many rotordynamic instability fiascos. The myriad of experimental results shown demonstrates that damper seals produce direct  $K$  and  $C$  orders of magnitude larger than those from conventional LSs. Damper seals in conjunction with a swirl brake also produce very small cross-coupled stiffnesses; hence, effectively removing any concerns about a possible induced rotordynamic instability, provided the seal cross-over frequency is below the first rotor-bearing system natural frequency. Past are the days when LSs, known *bad actors*, were the only choice to effectively sealing the stages in a turbomachine. Incidentally, damper seals, honeycomb and hole-pattern seals in particular, can produce a large centering stiffness ( $K \gg 0$ ) that makes a balance piston seal in a back-to-back centrifugal compressor act as a third bearing, hence increasing the first natural frequency of the rotor system. Most compressors featuring damper seals have too much damping; that is, their logarithmic decrement is well in excess of that for a normal machinery acceptance criterion ( $> 0.1$ ).

Although both the BFM and CFD model are quite accurate to predict leakage, they fall short to replicate the experimentally derived force coefficients of damper seals. At times, the direct damping is accurately predicted while the direct stiffness or the cross-coupled stiffness are not, or vice versa. The predictive methods still need improvement, hence the need of constant and continuous experimental verification. Differences between predictions and the measured seal force coefficients are likely due to the lack of fidelity in reproducing complex unsteady (highly turbulent) flows whose dynamic pressure acting on the rotor produces the seal reaction forces. This note provides simple formulas to estimate the range of expected direct stiffness ( $K$ ) and effective damping ( $C_{eff}$ ) applicable to damper seals. The formulas are empirically derived *rules of thumb*, likely to change in the not distant future.

Presently, the stiffness and damping force coefficients of gas damper seals can be tailored to effectively modify the stability and vibratory response of a turbomachine (compressor or turbine), even displacing the location of a critical speed. Properly designed clearance seals integrating swirl brakes are no longer a source of rotordynamic instability. As the energy market shifts toward carbon capture and hydrogen compression, accurate knowledge of aerodynamic forces from unshrouded compressors and open impellers will become necessary in multi-stage rotors.

## ACKNOWLEDGMENTS

The authors thank the teaching and mentoring imparted by Profs. John Vance and Dara Childs to countless students and practitioners of the art and science of rotordynamics. The two professors/engineers conducted monumental research on gas and liquid annular seals that aided to improve the stability and dynamic performance of centrifugal compressors. John and Dara made a formidable team, one that brought immense reputation to the TAMU Turbomachinery Laboratory. In an age of muscle-computer crunching, young engineers must continue to exercise critical thinking toward solving effectively problems in the simplest way, by applying Newton's Laws.

The authors acknowledge the multitude of students, graduate and undergraduate, whose analytical and experimental works made the Turbomachinery Laboratory a premier research center in the world. Thanks to Dr. Jing Yang for preparing some of the graphical art.

## NOMENCLATURE

|            |   |
|------------|---|
| $C_e$      | $c_d C_r = \frac{\dot{m} \sqrt{R_g T}}{\pi D P_m \sqrt{1 - PR^2}} = \frac{\sqrt{R_g} \bar{\Phi}}{\pi}$ . Seal effective clearance [m] |
| $C_{eff}$  | $(C - k/\omega)$ . Seal effective damping coefficient [N-s/m]   |
| $c_d$      | $(C_e / C_{r,step})$ . Seal leakage loss coefficient or fraction of physical clearance [-]  |
| $C, c$     | Direct and cross-coupled ( $i \neq j$ ) damping coefficients [N/m]  |
| $C_r$      | Seal nominal clearance [m]  |
| $D$        | Rotor diameter, tip diameter of blade [m]   |
| $F_x, F_y$ | Seal reaction forces in Cartesian coordinates [N]   |
| $F_r, F_t$ | Seal reaction forces in polar coordinates [N]   |
| $K, k$     | Direct and cross-coupled stiffnesses [N/m]  |
| $K_{eff}$  | $(K + c \omega)$ . Seal effective stiffness coefficient [N/m]   |

|                   |   |
|-------------------|---|
| $L$               | Seal axial length [m]   |
| $\dot{m}$         | Seal mass flow rate [kg/s]  |
| $P$               | Pressure [Pa]   |
| $P_{in}$          | Inlet pressure [Pa]   |
| $P_{out}$         | Exit (discharge) pressure [Pa]  |
| $PR$              | $P_{out}/P_{in}$ . Pressure ratio   |
| $Q$               | Volumetric flow rate [m <sup>3</sup> /s]  |
| $R_G$             | Air gas constant [J/(kg-K)]   |
| $t$               | Time [s]  |
| $T$               | Gas temperature [K]   |
| $U$               | Gas circumferential speed [m/s]   |
| $U_s$             | $\frac{1}{2} R D$ . Rotor surface speed [m/s]   |
| $\mu$             | Gas viscosity [cP]  |
| $\mu_i, \mu_{2i}$ | Coefficients in leakage equation  |
| $\phi$            | $\frac{\dot{m}\sqrt{T}}{D P_{in}}$ . Flow factor for seal ( $[kg \sqrt{K} / (MPa \cdot m \cdot s)]$ ) |
| $\bar{\Phi}$      | $\frac{\phi}{\sqrt{1-PR^2}}$ . Modified flow factor ( $[kg \sqrt{K} / (MPa \cdot m \cdot s)]$ )       |
| $\rho$            | Gas density [kg/m <sup>3</sup> ]  |
| $\omega$          | Excitation (whirl) frequency [rad/s]  |
| $\Omega$          | Shaft speed [rad/s]   |

## Abbreviations

|      |  |
|------|--|
| BFM  | Bulk flow model                        |
| CFD  | Computational fluid dynamics           |
| FPDS | Fully-partitioned PDS                  |
| HALO | Hydrostatic advanced low leakage seal  |
| HS   | Honeycomb seal                         |
| HoS  | Hole-pattern seal                      |
| LS   | Labyrinth seal                         |
| PDS  | Pocket damper seal                     |
| SB   | Swirl brake                            |
| WFR  | $k/((C\omega)$ . Whirl frequency ratio |

## REFERENCES

- [1] R. E. Chupp, R. C. Hendricks, S. B. Lattime, S. B. M. and M. F. Aksit, "Turbomachinery Clearance Control," *AIAA Turbine Aerodynamics, Heat Transfer, Materials, and Mechanics*, vol. 1, p. 61, 2007.
- [2] L. San Andrés, "Modern Lubrication Theory: Annular Pressure (Damper) Seals," College Station, 2009.
- [3] D. Childs, "Rotordynamic Models for Annular Gas Seals," in *Turbomachinery Rotordynamics: Phenomena, Modeling, and Analysis*, John Wiley & Son, 1993.
- [4] H. Black, "Effects of Hydraulic Forces on Annular Pressure Seals on the Vibrations of Centrifugal Pump Rotors," *J. Mechanical Engineering Science*, vol. 11, no. 2, pp. 206-213, 1969.
- [5] J. Alford, "Protecting Turbomachinery from Self-Excited Rotor Whirl," *Journal of Engineering for Power*, vol. 87, no. 4, pp. 333-343, 1965.
- [6] H. Benckert and J. Wachter, "Flow Induced Spring Coefficients of Labyrinth Seals for Application in Rotor Dynamics," in *Workshop on Rotordynamic Instability Problems in High-Performance Turbomachinery*, College Station, TX, 1980.
- [7] G. Von Pragenau, "Damping Seals for Turbomachinery," 1982.

- [8] D. Childs, D. Elrod and H. K., "Annular Honeycomb Seals: Test Results for Leakage and Rotordynamic Coefficients; Comparisons to Labyrinth and Smooth Configurations," *ASME Journal of Tribology*, vol. 111, no. 4, pp. 293-301, 1989.
- [9] D. Childs, D. Elrod and C. Ramsey, "Annular Honeycomb Seals: Additional Test Results for Leakage and Rotordynamic Coefficients," in *Proceedings of IFTOMM Third International Conference on Rotordynamics*, Lyon, France, 1990.
- [10] J. Vance and R. Shultz, "A New Damper Seal for Turbomachinery," in *Proceedings of 14th Vibration and Noise Conference*, Albuquerque, NM, 1993.
- [11] D. Childs and J. Vance, "Annular Gas Seals and Rotordynamics of Compressors and Turbines," in *Proc. of the 26th Turbomachinery Symposium*, College Station, TX, 1997.
- [12] U. Yèucel, "Leakage and Swirl Velocities in Labyrinth Seals," 1996.
- [13] F. Cangioli, G. Vannini and T. Chirathadam, "A Novel Bulk-Flow Model for Pocket Damper Seals," *ASME J. Eng. Gas Turbines Power*, vol. 142, no. 2, p. 011012, 2020.
- [14] H. Tennekes and J. Lumley, "Chapter 5," in *A First Course in Turbulence*, Cambridge, Massachusetts, and London, England, The MIT Press, 1972, pp. 149-164.
- [15] L. San Andrés, "Modern Lubrication Theory-Turbulence Flow in Thin Film Bearings: Characteristics and Modeling," College Station, 2021.
- [16] ANSYS, *Ansys Fluent User's Guide*, Canonsburg, PA, USA, 2021.
- [17] ANSYS, *Ansys CFX-Solver Modeling Guide*, Canonsburg, PA, USA, 2021.
- [18] J. Demko, G. Morrison and D. Rhode, "The Prediction and Measurement of Incompressible Flow in a Labyrinth Seal," *ASME J. Eng. Gas Turbines Power*, vol. 111, no. 10, pp. 697-702, 1989.
- [19] L. Wein, T. Kluge, J. Seume, R. Hain, T. Fuchs, C. Kähler and R. H. F. Schmierer, "Validation of RANS Turbulence Models for Labyrinth Seal Flows by Means of Particle Image Velocimetry," in *ASME Turbo Expo Digital Conference*, 2020.
- [20] S. Nishida, M. Iwasaki, N. Omura, K. Nakakita and T. Nakajima, "Visualization of Destabilization Force of Labyrinths Gas Seal Using Fast-Responding Pressure Sensitive Paint," in *ASME Turbo Expo Digital Conference*, 2021.
- [21] A. Pugachev, U. Kleinhans and M. Gaszner, "Prediction of Rotordynamic Coefficients for Short Labyrinth Gas Seals Using Computational Fluid Dynamics," *ASME J. Eng. Gas Turbines Power*, vol. 134, no. 6, p. 062501, 2012.
- [22] L. San Andrés, J. Yang and L. Xu, "On the Leakage, Torque and Dynamic Force Coefficients of an Air in Oil (Wet) Annular Seal: a CFD Analysis Anchored to Test Data," *ASME J. Eng. Gas Turbines Power*, vol. 141, no. 2, p. 021008, 2019.
- [23] I. Delgado and M. Proctor, "Continued Investigation of Leakage and Power Loss Test Results for Competing Turbine Engine Seals," in *42nd AIAA/ASME/SAE/ASEE Joint Propulsion Conference & Exhibit*, Sacramento, California, 2006.
- [24] L. San Andrés, J. Yang and R. Kawashita, "On the Effect of Clearance on the Leakage and Cavity Pressures in an Interlocking Labyrinth Seal Operating With and Without Swirl Brakes: Experiments and Predictions," *ASME J. Eng. Gas Turbines Power*, vol. 143, no. 3, p. 031003, 2021.
- [25] L. San Andrés and Z. Ashton, "Comparison of Leakage Performance in Three Types of Gas Annular Seals Operating at High Temperature (300°C)," *STLE Tribol T.*, vol. 53, no. 3, pp. 463-471, 2010.
- [26] L. San Andrés and A. Anderson, "An All-Metal Compliant Seal Versus a Labyrinth Seal: A Comparison of Gas Leakage at High Temperatures," *ASME J. Eng. Gas Turbines Power*, vol. 137, no. 5, p. 052504, 2015.
- [27] J. Justak and C. Doux, "Self-Acting Clearance Control for Turbine Blade Outer Air Seals," in *Proc. ASME Turbo Expo 2009*, 2009.
- [28] J. Justak, "Self-adjusting Non-Contacting Seal". Patent 8919781 B2, 2014.
- [29] J. Justak, "Hydrogen Compressor Seal Case Study - Utilizing HALO (Non-Contacting, Compliant) Inter-Stage, Impeller Eye, Buffer and Fail-Safe Seals," in *Proc. of the 42th Turbomachinery Symposium*, Houston, TX, 2013.
- [30] D. Stiles, J. Justak, M. Kuzdal, M. H., M. Sandberg, E. Wilcox and C. Rohrs, "Application of Dynamic Pressure-balanced Seals in a Multi-stage Centrifugal Compressor," in *Proc. of the 45th Turbomachinery Symposium*, Houston, TX, 2016.
- [31] B. Ertas, A. Delgado and G. Vannini, "Rotordynamic Force Coefficients for Three Types of Annular Gas Seals with Inlet Preswirl and High Differential Pressure Ratio," *ASME J. Eng. Gas Turbines Power*, vol. 134, no. 4, p. 042503, 2012.
- [32] N. Sheng, E. Ruggiero, R. Devi, J. Guo and M. Cirri, "Experimental and Analytical Leakage Characterization of Annular Gas Seals: Honeycomb, Labyrinth and Pocket Damper Seals," in *ASME Turbo Expo*, 2011.
- [33] J. Torres, L. San Andrés and J. Yang, "A Stepped Shaft Labyrinth Seal VS. A Pocket Damper Seal: Leakage and Dynamic Force Coefficients Under Wet Gas Operation," in *ASME Turbo Expo 2022*, Rotterdam, The Netherlands, 2022.
- [34] D. Childs, *Turbomachinery Rotordynamics With Case Studies*, Wellborn, TX: Minter Spring Publishing, 2013, pp. 319-450.

- [35] L. Baldassarre, A. Bernocchi, M. Fontana, A. Guglielmo and G. Masi, "Optimization of Swirl Brake Design and Assessment of its Stabilizing Effect on Compressor Rotordynamic Performance," in *Proceedings of the 43rd Turbomachinery Symposium, Turbomachinery Laboratory*, College Station, Texas, 2014.
- [36] J. Yang and L. San Andrés, "Making Better Swirl Brakes Using Computational Fluid Dynamics: Performance Enhancement from Geometry Variation," *ASME J. Eng. Gas Turbines Power*, vol. 144, no. 2, p. 021027, 2022.
- [37] B. Venkataraman, D. Moulton, M. Cave, C. Clarke, J. Moore, J. Wilkes and T. Eldridge, "Design and Implementation of Swirl Brakes for Enhanced Rotordynamic Stability in an Off-shore Centrifugal Compressor," in *Proc. of the Asia Turbomachinery & Pump Symposium, Turbomachinery Laboratory*, College Station, Texas, 2018.
- [38] J. Glienicke, "Experimental Investigation of the Stiffness and Damping Coefficients of Turbine Bearings and their Application to Instability Prediction," in *Proc. Instn. Mech. Engrs., 1966-67*, 1966.
- [39] L. San Andrés, "Modern Lubrication Theory: Experimental Identification of Bearing Force Coefficients," Texas A&M University Digital Libraries, College Station, 2021.
- [40] D. Childs, D. Elrod and K. Hale, "Annular Honeycomb Seals: Test Results for Leakage and Rotordynamic Coefficients; Comparisons to Labyrinth and Smooth Configurations," *ASME. J. Tribol.*, vol. 111, no. 2, p. 293–300, 1989.
- [41] J. Li, L., San Andrés and J. Vance, "A Bulk-Flow Analysis of Multiple-Pocket Gas Damper Seals," *ASME J. Eng. Gas Turbines Power*, vol. 121, no. 2, pp. 355-363, 1999.
- [42] J. Yang, L. San Andrés and X. Lu, "Leakage and Dynamic Force Coefficients of a Pocket Damper Seal Operating Under a Wet Gas Condition: Tests Versus Predictions," *ASME J. Eng. Gas Turbines Power*, vol. 141, no. 11, p. 111001, 2019.
- [43] T. Wu and L. San Andrés, "Leakage and Dynamic Force Coefficients for Two Labyrinth Gas Seals: Teeth-on-Stator and Interlocking Teeth Configurations. A Computational Fluid Dynamics Approach to Their Performance," *ASME J. Eng. Gas Turbines Power*, vol. 141, no. 4, p. 0425011, 2019.
- [44] M. Thorat and D. Childs, "Predicted Rotordynamic Behavior of a Labyrinth Seal as Rotor Surface Speed Approaches Mach 1," *ASME. J. Eng. Gas Turbines Power*, vol. 132, no. 11, p. 112504, 2010.
- [45] A. Delgado, L. San Andrés, J. Thiele, J. Yang and F. Cangioli, "Rotordynamic Performance of a Fully-Partitioned Damper Seal: Experimental and Numerical Results," in *Proc. of the 49th Turbomachinery Symposium, a Virtual Event*, 2020.